

Fully-Parabolized Prediction of Hypersonic Sonic Boom

Christian B. King*, Sean M. Skowron†, and Steven A. E. Miller‡
 University of Florida, Gainesville, Florida 32611-6250

Hypersonic flight-vehicles create shock and expansion waves that propagate through the atmosphere and are observed on the ground as sonic booms. We present a methodology to predict the near-field aerodynamic pressure and sonic boom signature using approximately 1% of the computational cost relative to fully-nonlinear computational fluid dynamics and state-of-the-art sonic boom propagation solvers. Relative differences in predictions between the present method and the state-of-the-art are approximately 8%. We find that unique physics must be accounted for in the hypersonic regime, which includes viscous, non-equilibrium, and real gas effects. The method is based on the fully-parabolized Navier-Stokes equations, which are solved via marching in the propagation direction to the aerodynamic near-field. The near-field aerodynamic pressure is propagated through the atmosphere to the ground via the waveform parameter method, and is validated with NASA PCBoom and data from the NASA Sonic Boom Workshops. To illustrate the approach, three bodies are analyzed: the Sears-Haack geometry, the HIFiRE-5 hypersonic test vehicle, and a power-law waverider. Global Mach numbers range from 4.0 through 15.0. We find that the viscous stress tensor is essential for accurate hypersonic prediction. For example, viscous effects increase near-field and sonic boom overpressure by 15.7% and 8.49%, respectively for the Sears-Haack geometry. Finally, we show that the divergence of viscous versus inviscid near-field predictions are due to the hypersonic boundary layer.

Nomenclature

Symbols	Description	ω	Frequency
A	Local ray-tube area	ω'	Variable of integration
c	Speed of sound	ϕ	Azimuthal coordinate
D	Drag	θ_c	Surface inclination angle
$\mathbf{E}, \mathbf{F}, \mathbf{G}$	Streamwise flux vectors		
F	F-function	Non-Dimensional Numbers	
H	Atmospheric height	c_l	Lift coefficient
h	Vehicle altitude	c_s	Species mass fraction
k_B	Boltzmann constant	\bar{D}	Binary diffusion coefficient
L	Body length	e	Eccentricity
m	Slope of waveform segment	M	Mach number
p	Static pressure	\mathcal{K}	Hypersonic similarity parameter
p_∞	Freestream pressure	$\hat{\omega}_s$	Nondimensional production
p_g	Pressure at ground		
\bar{p}	Fourier transform of scaled acoustic pressure	Abbreviations	
r	Source cylinder radius	CFD	Computational Fluid Dynamics
s	Ray path length	PNS	Parabolized Navier-Stokes
s_l	Streamwise position	UPS	Upwind Parabolized Navier-Stokes Solver
U	Velocity magnitude	IPNS	Iterative Parabolized Navier-Stokes
U_∞	Freestream velocity magnitude	WPM	Waveform Parameter Method
Greek Symbols		Superscripts	
α_t	Effective absorption coefficient	p	Elliptic regime
β	Coefficient of non-linearity	*	Parabolic-hyperbolic regime
β_p	Prandtl-Glauert factor		
γ	Ratio of specific heats	Subscripts	
δ^*	Displacement thickness	c	Cone surface
ξ, η, ζ	Transformed coordinates	∞	Ambient condition
λ	Time duration of waveform segment		

*Ph.D. Student, Department of Mechanical and Aerospace Engineering, christianking@ufl.edu, AIAA student member.

†Undergraduate Researcher, Department of Mechanical and Aerospace Engineering, seanskowron@ufl.edu, AIAA student member.

‡Associate Professor of Mechanical and Aerospace Engineering, Theoretical Fluid Dynamics and Turbulence Group, Department of Mechanical & Aerospace Engineering, University of Florida, 331 MAE-A, P. O. Box 116250, Gainesville, FL 32611, saem@ufl.edu; saemiller@gmail.com, AIAA Senior and lifetime member.

I. Introduction

FLIGHT-vehicles traveling at hypersonic speeds create shock waves and expansion fans that propagate nonlinearly through the atmosphere as sonic booms. To aid in the design and development of high-speed flight-vehicles, it is important to quickly resolve the flow-field using fast flow solvers to minimize design time. Fast and accurate prediction of low-thickness ratio or bluff body flight-vehicles can Multi-Disciplinary Analysis and Optimization (MDAO) design time and enable ultra fast prediction to determine the sonic boom footprint. This way, flight-vehicles can be assessed before higher fidelity computational fluid dynamics (CFD) is performed. Fast flow-field solvers make assumptions that drastically decrease computational cost and wall-clock time at the expense of solution fidelity. Therefore, their accuracy must be compared with fully nonlinear CFD solvers or experimental measurements to validate prediction quality. Prediction of near-field source pressure for sonic boom propagation often is performed using tools such as NASA's FUN3D CFD solver [1]. The near-field is defined as the region outside the vorticity induced by the flight-vehicle. Current methods such as adjoint-based mesh adaptation of Park [2, 3] show significant improvements for near-field prediction by minimizing uncertainty of error estimates. We accurately predict hypersonic near-field signatures and sonic boom using a fully-parabolized approach.

In this study, we predict the source near-field via spatially marching solutions of the Parabolized Navier-Stokes (PNS) equations and predict sonic boom at the ground via the Waveform Parameter Method (WPM) [4, 5]. We demonstrate that we can achieve nearly equivalent solution quality using fully-parabolized near-field and sonic boom prediction methods relative to industry standard approaches. Furthermore, the wall-clock time of the present approach is reduced by up to two orders of magnitude [6]. We are also able to capture the effect of chemically reacting non-equilibrium flows, which are important for hypersonic calculations. The present paper investigates the effects of viscosity and non-equilibrium reacting flow on the hypersonic near-field and sonic boom at the ground for three hypersonic vehicles: The Sears-Haack [7] geometry, a HIFiRE-5 [8] hypersonic test vehicle, and a power-law waverider [9].

A. Previous Approaches

Previously, two major analytical approaches were developed for predicting the near-field. The methods of Whitham [10, 11] and Carlson [12] are based on linearized aerodynamic theory. These methods predict the near-field using a closed-form integral equation, which includes the so-called F-function in the integrand. The formulation of these methods is similar and often confused with the area rule, which was initially developed by Vera Maslennikova in the Soviet Union and later by Whitcomb and Fischetti [13] and Whitcomb [14] in the United States. Unfortunately, these theories are restricted to slender flight-vehicles with freestream Mach numbers, M_∞ , between 1.2 and 3.0, as noted by Hayes [15] and Hayes and Runyan [16]. For bluff-body hypersonic flows, Seebass [17] and Tiegerman [18] developed an instantaneous impulse method that is applicable to high-speed flows over an infinitely long fuselage that does not generate lift. Their models account solely for flight-vehicle volume, which contributes to over 40% [19] of the sonic boom overpressure at moderate supersonic to hypersonic speeds. Housman et al. [20] predict near-field pressure signatures by spatially marching the Euler equations to an extraction point.

The F-function (see Whitham [10, 11] and Carlson [12, 21]) relies on linearized supersonic theory and corrections for lift. Specifically, the F-function is an argument of an integral equation for the pressure time history in the flight-vehicle near-field. Typically, this pressure time history is propagated through the atmosphere with contemporary sonic boom propagation solvers. The theory leads to the basic equation for static pressure about the atmospheric pressure

$$\Delta p(x - \beta_p r, r) = \frac{p_\infty \gamma M^2 F(x - \beta_p r)}{(2\beta_p r)^{1/2}}, \quad (1)$$

where p is pressure, p_∞ is ambient pressure, r is the radius, M is the Mach number, x is the axial coordinate, β_p is the Prandtl-Glauert factor, and γ is the ratio of specific heats. The F -function is

$$F(x) = \frac{1}{2\pi} \int_0^x \frac{A''(\xi)}{(x - \xi)^{1/2}} d\xi, \quad (2)$$

and A is modified by Cramer [22] as

$$A_L(x, \theta) = \frac{\beta_p}{\rho u_\infty^2} \int_0^x L(x, \theta) dx, \quad (3)$$

to account for lift. Here, L is the component of lift per unit length and A_L is the modified area. At hypersonic Mach numbers the error increases, and the F-function is no longer applicable. Even though the F-function accounts for lift and is designed for slender bodies, the disagreement at hypersonic speeds is unacceptable. Linearized theory (F-function method with corrections for lift) is unable to account for hypersonic Mach numbers, and the error is compounded with the addition of lift. This error is primarily due to the nonlinear nature of hypersonic flow-fields. F-function theory does not provide satisfactory predictions at $M_\infty > 3$ with or without non-zero lift. Example predictions are shown in Morris et al. [23] and Hunton [24], where predictions depart from theory at high-speeds.

An alternative method was formulated to overcome the limitations of the F-function approach at a hypersonic flight-vehicle Mach number. It was pioneered by Seebass [17] and uses the instantaneous energy pulse method. It was later extended in the Ph.D. dissertation of Tiegerman [18] and by Cramer [22], who performed an analysis with similarity and scaling laws to match the near-field flow to the far-field, where the method of Whitham [10] applies. The method works well for hypersonic flows for bluff bodies with zero lift. It cannot be applied to slender hypersonic bodies or lifting bodies.

Recently, Miller [25] proposed a new analytical method in two-dimensions to predict the near-field. However, the method relies on constructing complicated source and propagation functions that are difficult to ascertain for complex flight-vehicle configurations. We hope that in the future, this newly developed analytical method will replace the present and other approaches entirely.

Experiments can capture near-field pressure, but they are very costly and measurement is difficult [26–28]. Near-field pressure can be measured in a wind-tunnel [29]; however, the near-field required for sonic boom propagation is often contaminated by wind tunnel wall effects. This results in measurements that are made too close to the model flight-vehicle for sonic boom propagation codes (see Carlson [12], Morgenstern [30], and Carlson and Morris [31]).

CFD can successfully predict the near-field pressure [32–34], but it is computationally expensive. This makes fully nonlinear CFD undesirable for MDAO, which requires rapid prediction. Generally nonlinear CFD solvers, that often use adjoint based grid adaptation, are computationally expensive. They are emerging as the industry standard for near-field sonic boom source prediction.

Typically, computational domains for near-field prediction are much higher than typical aerodynamic predictions, and grid points per condition are approximately on the order of 10^8 . Shock waves must be resolved, which greatly increases the problem complexity. Adaptive grids are often used to capture shock waves far from the flight-vehicle. The volume of the domain must also be large as to contain the source cylinder for the propagation solver, and the domain must extend well outside the induced vorticity field. Typically, the near-field should be extended by multiple body lengths in the cross-stream direction to conduct a proper sonic boom prediction. Unfortunately, this means that the computational domain must resolve shock and expansion waves accurately with little dissipation and dispersion error. This has continued to challenge the community for decades. Recent advances in sonic boom near-field prediction have been made by the research conducted under the NASA X-59 program. For example, recent CFD advances for NASA X-59 are presented by Park and Carter [35]. However, these advances have focused on sonic boom for commercial aircraft in the supersonic regime and not for hypersonic flight-vehicles.

These near-field pressure waveforms must be propagated to the ground through the atmosphere. There are multiple contemporary solvers for this purpose and are generally called sonic boom solvers. These include sBOOM by Rallabhandi [36] and PCBoom by Plotkin et al. [37]. These are the most advanced contemporary sonic boom propagation solvers available to the present investigators, are highly validated, used throughout industry and government, and represent the state-of-the-art.

The prediction methodologies for the near-field and sonic boom are explained in Sec. II. Results and analyses of hypersonic near-field and sonic boom are presented in Sec. III. The summaries and conclusions of this research are in Sec. IV.

II. Prediction Methodology

We use a fully-parabolized marching solver to predict the flow-field of a hypersonic flight-vehicle. The near-field for slender, hypersonic flight-vehicles, is in the range of $rL^{-1} = 0.15$ to $rL^{-1} = 1.0$ (see Loubeau and Coulouvrat [38]). Here, r is the radial position from the centerline of the flight-vehicle, and L is the length of the flight-vehicle. The near-field represents the region as close to the flight-vehicle as possible, but outside the region of induced vorticity. Higher fidelity near-field predictions are made by accounting for viscosity in the cross-flow directions as well as including finite-rate air chemistry.

Figure 1 presents the prediction approach. Here, the source cylinder (top), the near-field pressure (middle), and

the ground waveform (bottom) are shown. A generic flight-vehicle is shaded grey. Flow moves from left to right. The source cylinder is located at r . The source cylinder represents the mathematical surface that encompasses the flight-vehicle where pressure is measured or predicted in the near-field. Strong leading and trailing shock waves will be attached to the vehicle, shown as solid and dashed lines, respectively. There are many shock and expansion waves in between. In the parabolized approach, solutions are marched downstream and terminate when they intersect the source cylinder at location, r . Solutions are initialized from the free-stream in front of the flight-vehicle. We normalize the local static pressure, p , relative to the local ambient pressure, by the ambient pressure, p_∞ . This near-field source cylinder, that is a function of azimuthal angle, ϕ , is propagated to the ground to predict the footprint of the hypersonic flight-vehicle. It is very typical that hypersonic flight-vehicles, even at low altitude, produce strong over-pressure and N-waves at the ground, which are represented at the bottom of Fig. 1. We use both WPM and PCBoom to predict sonic boom propagation and the sonic boom footprint (ground signature).

Figure 2 shows a flow-chart of the prediction process. The solver requires that we specify the shape of the vehicle. The domain of the solution is constructed by the solver automatically as it marches downstream. Here, at minimum we define the flight-vehicle half-angle, θ_c , cross-section eccentricity, e , and the body length, L to construct a simplified geometry. A grid spreading angle is determined by the user and is bounded by the leading shock wave angle. The computational domain is algebraically generated within the solver. This angle is larger than the Mach angle of the ambient flow-field to guarantee that shock waves do not intersect the outer edge of the grid. The flow-field is calculated by solving the PNS equations, which are closed by equilibrium, finite-rate non-equilibrium, or frozen air chemistry [39–41] models. The ratio, pp_∞^{-1} , at a specified source-cylinder radius is then extracted for the sonic boom solver.

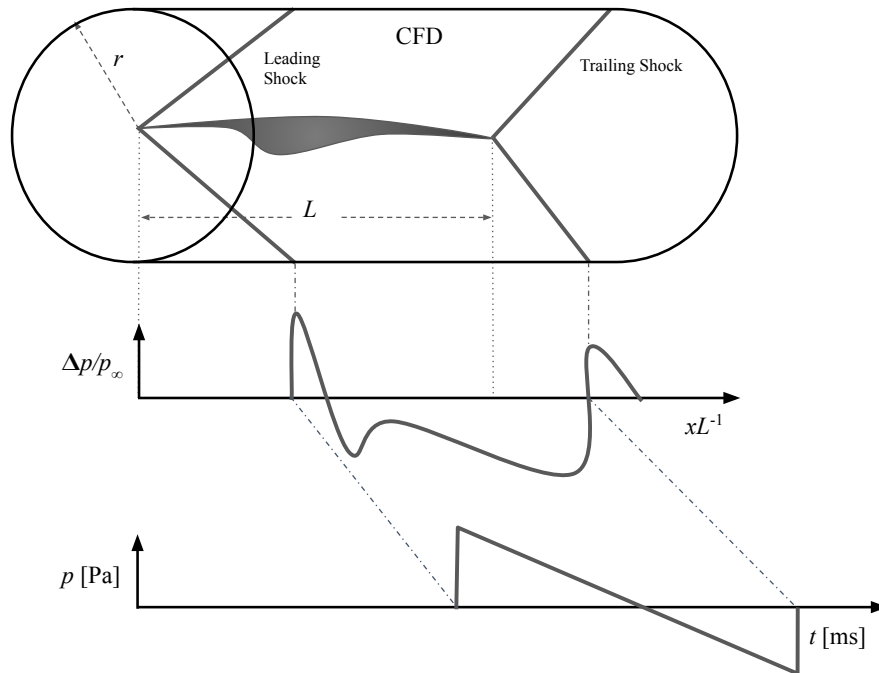


Fig. 1 Geometry, source cylinder, near-field pressure, and sonic boom signature.

A. Upwind Parabolized Navier-Stokes Solver

We present the PNS equations that model the hypersonic near-field and associated numerical solution approach. The PNS equations are derived from the Navier-Stokes equations by assuming unsteady and viscous derivatives to be zero [42]. The PNS equations are

$$\frac{\partial \mathbf{E}}{\partial \xi} + \frac{\partial \mathbf{F}}{\partial \eta} + \frac{\partial \mathbf{G}}{\partial \zeta} = 0, \quad (4)$$

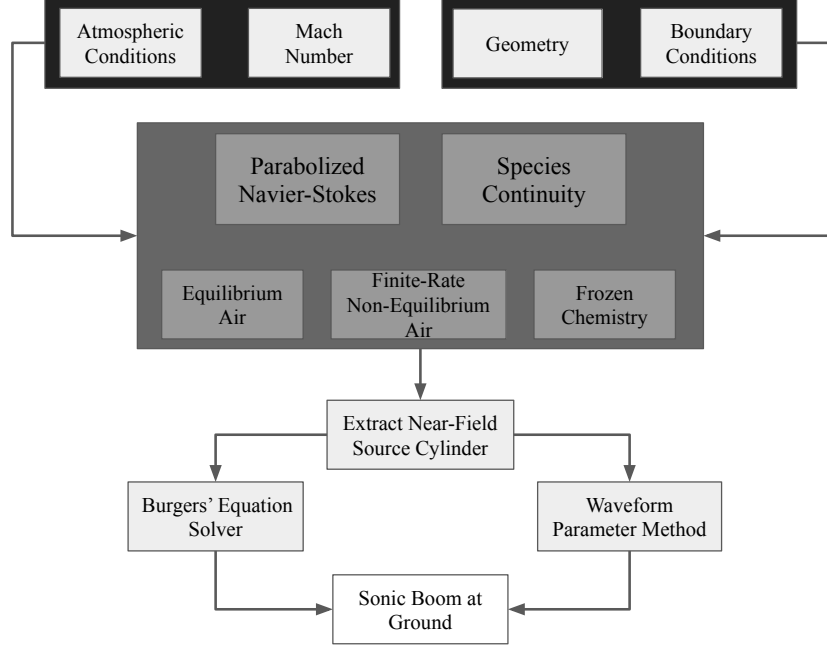


Fig. 2 Fully-parabolized prediction system.

where E , F , and G are the flux vectors in the ξ , η , and ζ directions, respectively.

The PNS equations are parabolic-hyperbolic in the ξ -direction if the local flow-field is supersonic. In subsonic regions (elliptic) of the flow-field, departure behavior is restrained by employing the technique of Vigneron et al. [43]. Vigneron's technique separates the streamwise flux vector into two terms, where E^P is the elliptic portion and E^* is the parabolic-hyperbolic portion. This is represented as

$$\mathbf{E} = \mathbf{E}^* + \mathbf{E}^P. \quad (5)$$

Using forward differencing, the streamwise flux gradient is

$$\left(\frac{\partial \mathbf{E}}{\partial \xi} \right)_{i+1} = \frac{1}{\Delta \xi} [\mathbf{E}_{i+1}^* - \mathbf{E}_i^* + \mathbf{E}^P(d\mathbf{S}_{i+1}, \mathbf{U}_{i+2}) - \mathbf{E}^P(d\mathbf{S}_i, \mathbf{U}_{i+1})]. \quad (6)$$

Streamwise and cross-stream flux gradients are then linearized and substituted into the PNS equations (see Eqn. 4) and the Iterative PNS (IPNS) method of Miller et al. [42] is implemented to improve predictions in regions with upstream influence. The full discretized form of the equations is

$$\begin{aligned} & \left\{ \frac{1}{\Delta \xi} [A^*(d\mathbf{S}_{i+1}, \mathbf{U}_i) - A_i^P]^{k+1} + \frac{\partial}{\partial \eta} \left[\frac{\partial \mathbf{F}(d\mathbf{S}_{i+1}, \mathbf{U}_i)}{\partial \mathbf{U}} \right]^{k+1} + \frac{\partial}{\partial \zeta} \left[\frac{\partial \mathbf{G}(d\mathbf{S}_{i+1}, \mathbf{U}_i)}{\partial \mathbf{U}} \right]^{k+1} \right\} \Delta \mathbf{U}_i^{k+1} \\ & = -\frac{1}{\Delta \xi} \{ [A(d\mathbf{S}_{i+1}, \mathbf{U}_i) - A_i]^{k+1} \mathbf{U}_i^{k+1} - \mathbf{E}^P(d\mathbf{S}_{i+1}, \mathbf{U}_{i+2})^k + \mathbf{E}^P(d\mathbf{S}_{i+1}, \mathbf{U}_i)^{k+1} \} \\ & \quad - \left[\frac{\partial \mathbf{F}(d\mathbf{S}_{i+1}, \mathbf{U}_i)}{\partial \eta} \right]^{k+1} - \left[\frac{\partial \mathbf{G}(d\mathbf{S}_{i+1}, \mathbf{U}_i)}{\partial \zeta} \right]^{k+1}. \end{aligned} \quad (7)$$

The Upwind Parabolized Navier-Stokes Solver (UPS) is used to predict flow-fields for flight-vehicles and is originally based on Lawrence et al. [4]. UPS has the ability to predict ideal, real, and non-equilibrium reacting flow-fields

[44]. UPS employs the real gas model implemented by Tannehill et al. [40] to resolve chemically reacting flows. For non-equilibrium flows, the species continuity equation employed by Tannehill et al. [39] is solved. The non-dimensional species continuity equation is

$$\frac{\partial c_s}{\partial \xi} + \left(\eta_x + \frac{v}{u} \right) \frac{\partial c_s}{\partial \eta} = \frac{1}{\rho u} \left[\dot{\omega}_s + \frac{\eta_y}{\text{Re}_\infty} \frac{\partial}{\partial \eta} \left(\beta_3 \rho \tilde{D} \eta_y \frac{\partial c_s}{\partial \eta} \right) + \frac{\eta_x}{\text{Re}_\infty} \frac{\partial}{\partial \eta} \left(\beta_3 \rho \tilde{D} \eta_x \frac{\partial c_s}{\partial \eta} \right) + \frac{\delta}{y} \frac{\eta_y}{\text{Re}_\infty} \left(\beta_3 \rho \tilde{D} \frac{\partial c_s}{\partial \eta} \right) \right], \quad (8)$$

where the governing equation for species continuity is a function of species mass fraction, c_s , non-dimensional production, $\dot{\omega}_s$, binary diffusion coefficient, \tilde{D} , freestream Reynolds number, Re_∞ , and β , where $\beta = (k_B T)^{-1}$ (see Tannehill et al. [41] for details). Near-field prediction validations using UPS have previously been performed by King and Miller [6].

B. PCBoom

We use two sonic boom solvers. PCBoom is used to validate and compare predictions of various source waveforms with those predicted with WPM. PCBoom has a long and prestigious history within the aeronautics community, and many iterations of the solver have been published (see Salvetti and Seidman [45] and Plotkin [19] for details). We use the version of PCBoom presented by Lonzaga [46]. The solver is based on the traditional idea of finding rays through the atmosphere, and then subsequently propagating the source waveform to the ground along these rays. In the present formulation of Lonzaga [46], a propagation equation is numerically integrated and is

$$\frac{d\tilde{p}}{ds} = \frac{i\omega\tilde{\beta}}{4\pi} \int_{-\infty}^{\infty} \tilde{p}(s, \omega') \tilde{p}(s, \omega - \omega') d\omega' - \alpha_t(s, \omega) \tilde{p}(s, \omega), \quad (9)$$

where \tilde{p} is the Fourier transform of the scaled acoustic pressure, s is the ray path length, α_t is the effective absorption coefficient, $\tilde{\beta}$ is the scaled coefficient of non-linearity, and ω is the frequency. The variable of integration is ω' . For predictions, we use the FOBoom module within version 7.1 of PCBoom. The ray path solver includes the ray velocity, slowness vector, and Doppler shift effect. The solver computes the evolution of the sonic boom signature using a Middle-Carlson-Hayes age parameter [47].

C. Waveform Parameter Method

WPM is an alternative propagation method relative to PCBoom. The approach is based on the research of Thomas [5], and was compared with other methods by Cleveland et al. [48]. This method eliminates the requirement for area balancing to determine shock wave location used by other methods, while being mathematically equivalent to it (similar assumptions are used in the derivation). The methodology represents a semi-closed-form set of equations. To close the equations, we identify the shock-coalescence positions along the path from the flight-vehicle to the ground. Each step of the propagation solver occurs at these shock-coalescence positions. Therefore, it is possible that a single step of the solver can occur between source and observer. This is advantageous for fast parabolic solver techniques, which can potentially reduce computational cost of MDAO analysis.

Three major equations are advanced after solving for the propagation path, s , via ray-theory. The first differential equation tracks the evolution of the local slope of each waveform segment, m , as

$$\frac{dm_i}{dt} = c_1 m_i^2 + c_2 m_i, \quad (10)$$

where i is the segment number and t is waveform time. Auxiliary functions c_1 and c_2 are defined below. Increase in p due to shock waves is tracked by Δp and governed by

$$\frac{d\Delta p_i}{dt} = \frac{1}{2} c_1 \Delta p_i (m_i + m_{i-1}) + c_2 \Delta p_i, \quad (11)$$

where p is the local static over-pressure. Finally, the duration of each segment is tracked and is defined as λ_i , which evolves according to

$$\frac{d\lambda_i}{dt} = -\frac{1}{2}c_1 (\Delta p_i + \Delta p_{i+1}) - c_1 m_i \lambda_i. \quad (12)$$

Auxiliary functions c_1 and c_2 are

$$c_1 = \frac{\gamma + 1}{2\gamma} \frac{c_\infty}{p_\infty c} \text{ and } c_2 = \frac{1}{2} \left(\frac{3}{c_\infty} \frac{dc_\infty}{dt} + \frac{1}{\rho_\infty} \frac{d\rho_\infty}{dt} - \frac{2}{c_n} \frac{dc}{dt} - \frac{1}{A} \frac{dA}{dt} \right), \quad (13)$$

respectively. Here, A is the local ray-tube area at the waveform position along the ray path, c is the local ambient speed of sound, γ is the ratio of specific heats, and ρ is the local density.

Source cylinder waveforms from CFD, experiment, or analytical theory provide p versus τ or x . These waveforms must be parameterized for WPM. It is easy to discretize these initial waveforms and quickly approximate each segment with corresponding slopes, m , duration, λ , and over-pressures, Δp . Note that Δp is zero unless a discontinuity occurs, which is denoted by $\lambda = 0$. The original WPM developed at NASA has been improved through conversion to contemporary Fortran. WPM is compatible with source cylinders generated from FUN3D and the fully-parabolized approach previously described. This makes WPM a more versatile and fast sonic boom solver for integration with parabolized approaches and MDAO analysis.

D. Sonic Boom Signal Processing

We present sonic boom spectra in the form of SPL per unit Hz in addition to time domain predictions of sonic boom. These spectra can be interpreted as the amount of energy per unit bandwidth in the waveform at frequency, f . Low frequency resolution is increased via mirroring (creating additional periodic instances of the waveform). Each waveform contains 16 periods. Waveforms are zero-padded and interpolated onto a constant time step for calculation of energy spectral density (ESD). ESD is calculated via the discrete Fourier transform and its associated complex conjugate. Sound pressure level (SPL) is calculated via $\text{SPL} = 10 \log_{10} [\text{FT}(p)\text{FT}^*(p)/p_{\text{ref}}^2]$. Here, FT is the Fourier transform, superscript $*$ represents the complex conjugate, and p_{ref} is the reference pressure of 20 μPa .

III. Results

We first present the sonic boom prediction validation of WPM with PCBoom and data from the NASA/AIAA Second Sonic Boom Prediction Workshop. Next, grid independence studies for prediction of the aerodynamic near-field are presented. Parabolized predictions for the near-field and sonic boom from three major configurations are analyzed: the Sears-Haack geometry [7], the HIFiRE-5 hypersonic flight-vehicle, and a power-law waverider. In each case, the near-field pressure and sonic boom waveform are predicted. Near-field and sonic boom signature alterations resulting from viscosity and non-equilibrium effects are analyzed and presented.

A. Validation of Waveform Parameter Method with PCBoom and NASA/AIAA Sonic Boom Prediction Workshop

Predictions of WPM are validated with PCBoom and the averaged consensus predictions of the 2nd AIAA Sonic Boom Workshop [49]. The ground track from both the Lockheed-Martin (LM) 1021 and the axisymmetric, equivalent area configurations are propagated using WPM and PCBoom. These two predictions are then compared with the workshop consensus predictions. Each sonic boom prediction is performed at a latitude of 34 deg. All sonic boom predictions use a ground reflection factor of 1.90.

PCBoom is a suite of sonic boom prediction methodologies. The FOBoom module within PCBoom is used to propagate the zero azimuth, $\phi = 0$ deg., of the source waveform to the ground. PCBoom uses T , p , and \bar{u} (horizontal wind) as a function of altitude to account for the atmosphere. The wind velocity vector is decomposed into two components: north and east. Vertical wind is not accounted for in WPM or PCBoom. Like PCBoom, WPM uses the same profiles of T and p . However, WPM calculates pressure as a function of altitude using a gas law. Note that public availability of sonic boom measurements are limited, if not non-existent at $M_\infty > 5$, especially for slender hypersonic waveriders.

Three atmospheric profiles are examined for each sonic boom validation case, which include the standard atmosphere without wind, and two atmospheres with varying thermodynamic properties and wind. For the LM1021 predictions, two atmospheric profiles are obtained from Green Bay, WI in February [50], labeled ‘Atmosphere 1’ and

‘Atmosphere 2’ in Fig. 3a and 3b, respectively. For these latter cases, predictions of sonic boom are located at the ground, which is 214.0 m above sea-level. The axisymmetric case is run with Atmosphere 3, measured at the NASA Wallops Flight Facility, where the ground elevation is 13.0 m. Finally, Atmosphere 4 is measured at Edwards Air Force Base, where the elevation is 724.0 m. Both of these atmospheric profiles were recorded in August [50].

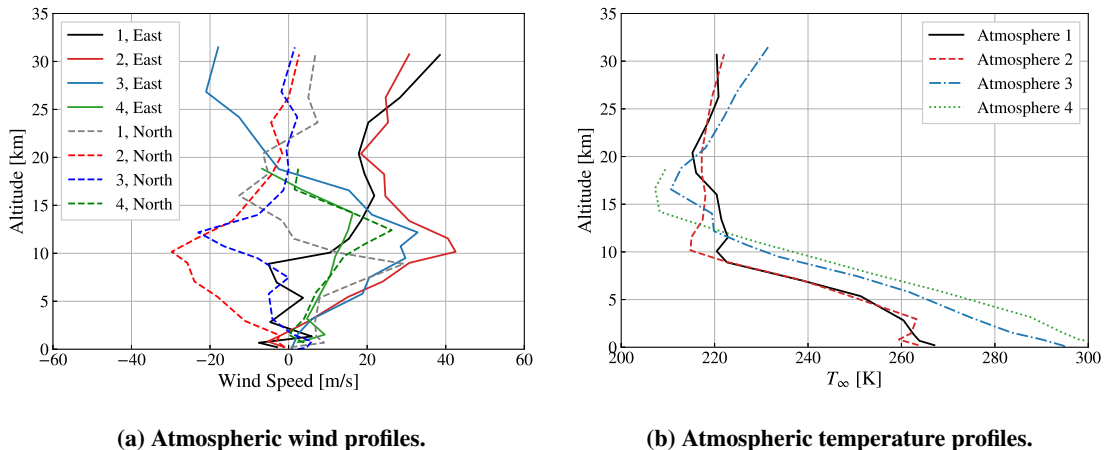


Fig. 3 Measured atmospheric profiles for sonic boom propagation validation.

A sonic boom prediction validation is presented for the LM 1021 low-boom concept. The LM1021 validation case has a flight-vehicle length of $L = 71.117$ m, flies at $M_\infty = 1.60$, and has an altitude of 16.764 km. Figure 4a shows the near-field prediction of the under-track, where $\phi = 0.0$ deg. and $rL^{-1} = 3.1299$ (see Morgenstern [30] for details). Figures 4b through 4d show the ground pressure signature through each of the three atmospheric profiles, respectively. PCBoom predicts a maximum overpressure of 57.47 Pa. WPM predicts a maximum overpressure of 53.24 Pa, which is approximately 7.4% lower than PCBoom’s prediction. WPM’s prediction nearly matches the mean peak overpressure of the NASA Sonic Boom Workshop, which is 53.20 Pa [49]. WPM predicts a minimum pressure of -39.33 Pa at $t = 211.79$ ms as compared to PCBoom’s prediction of -41.88 Pa at $t = 213.24$ ms. Relative to PCBoom, WPM predicts the amplitude to be 6% lower with a corresponding 0.68% shorter interval. Mean minimum pressure predicted by the workshop [49] is -37.56 Pa at 209.46 ms. Overall, for this case, predictions of ground static pressure are in relative quantitative agreement. WPM performed quantitatively better than PCBoom in predicting duration and over-pressure relative to the NASA Sonic Boom Workshop dataset for this particular case. Note that WPM cannot predict shock wave thickness. The hypersonic community is generally interested in duration and overpressure, and the cost savings from using a parameter method are advantageous computationally.

We now validate the predictive capabilities of WPM and PCBoom with the axisymmetric, equivalent area configuration. This configuration represents a low boom concept that was part of the 2nd AIAA/NASA Sonic Boom Prediction Workshop (see Rallabhandi and Loubeau [49] for details). Figure 5a shows the near-field prediction at $\phi = 0.0$ deg., $rL^{-1} = 3.0$, of the axisymmetric body at $M_\infty = 1.60$ and 15.850 km altitude. The flight-vehicle length is $L = 42.98$ m. Similar to the LM1021 case, the near-field is propagated through a standard atmosphere with 70% humidity and Atmospheres 3 and 4, as previously shown in Fig. 3. Predictions of WPM for sonic boom at the ground are benchmarked against predictions of PCBoom and the mean results of Rallabhandi and Loubeau [49]. For the case with the standard atmospheric profile in Fig. 5b, WPM predicts maximum pressure at the ground to be 22.92 Pa at 34.28 ms. In contrast, PCBoom predicts maximum pressure to be 24.00 Pa at 33.45 ms, and the mean prediction of Rallabhandi and Loubeau [49] is 20.61 Pa at 37.01 ms. The WPM prediction is 4.5% lower in magnitude and 9.6% earlier in time than the PCBoom prediction. Here, WPM’s prediction of the value of the overpressure and its time is closer to the mean prediction than PCBoom’s by 31.9% and 23.3%, respectively. Minimum predicted p by WPM, PCBoom, and Rallabhandi and Loubeau [49] are -13.55 Pa at 113.64 ms, -14.18 Pa at 113.90 ms, and -11.82 Pa at 112.62, respectively. WPM’s prediction is 4.4% lower in magnitude and 0.2% earlier in time than PCBoom’s. Like the previous benchmark, WPM predicts the ensemble averaged waveform of the NASA Sonic Boom Prediction Workshop [49] more accurately than PCBoom. Specifically, WPM predicts the magnitude of p with an accuracy of 26.7% and t with an accuracy of 20.3%, relative to PCBoom for the test dataset.

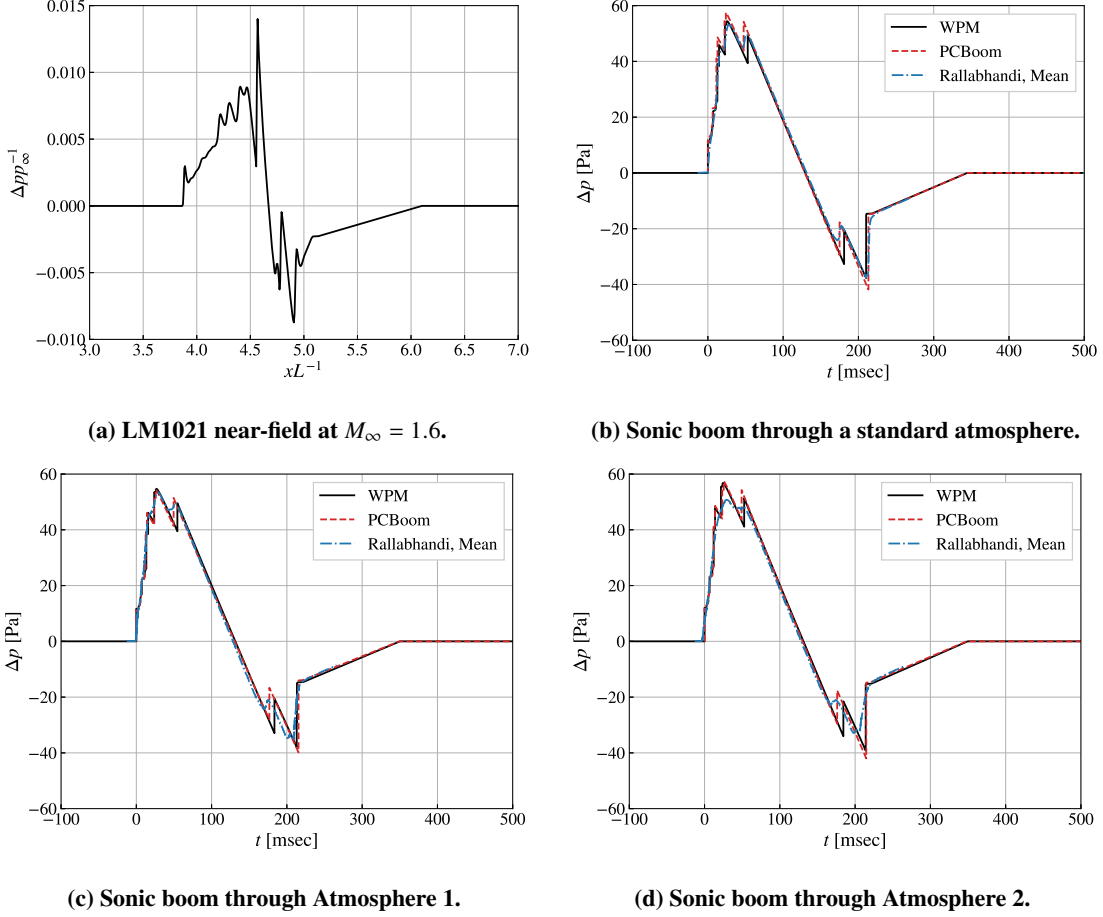


Fig. 4 Sonic boom validation for the LM1021 low-boom concept.

B. Geometries Investigated

We examine three fundamental geometries to understand the physics, near-field waveforms, and sonic boom from hypersonic flight-vehicles. They are the Sears-Haack [7] geometry, the HIFiRE-5 hypersonic test vehicle, and a power-law waverider. These are chosen so that we can understand the effect of symmetry and lift on the near-field and sonic boom.

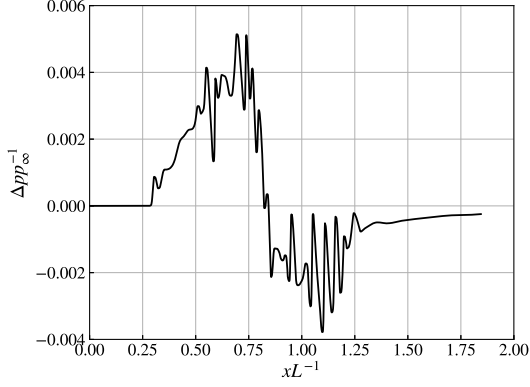
The equation that defines the Sears-Haack geometry is

$$r(x) = r_{\max} \left[\frac{4x}{l} \left(1 - \frac{x}{l} \right) \right]^{\frac{3}{4}}, \quad (14)$$

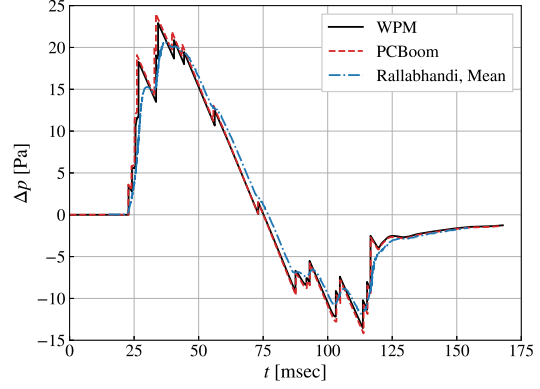
where $r(x)$ is the geometry surface radius, which depends on position, x , body length, l , and maximum body radius, r_{\max} . The Sears-Haack geometry parameters are chosen to match the study of Bantle [51], where the body length, $l = 0.762$ m, the maximum radius is $r_{\max} = 0.0261$ m, and the near-field source cylinder is $rL^{-1} = 0.3937$.

The HIFiRE-5 is a hypersonic flight-test vehicle on which three-dimensional aerothermodynamic effects were tested. All parameters of the HIFiRE-5 geometry examined in this study are identical to that of Juliano et al. [52], with the exception of a sharp leading edge and a trailing tail of -3.20 deg. from $x = 1.81$ to $x = 3.62$ m. After which, the geometry terminates and a trailing shock wave radiates. These slight modifications of the geometry are made to conform to requirements of the parabolized solver.

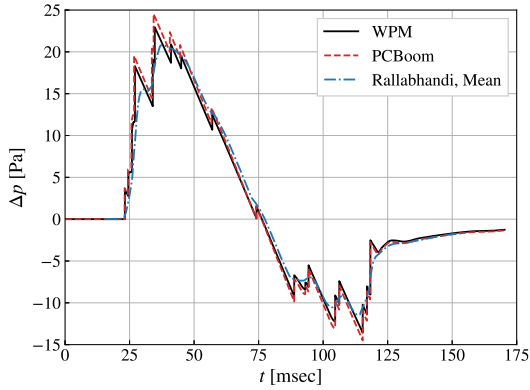
The third major geometry examined is the variable wedge angle (VWA) power-law waverider. A VWA waverider uses three governing power-law equations presented by Starkey and Lewis [9], which define the forebody of the waverider. Three equations define the VWA geometry and are



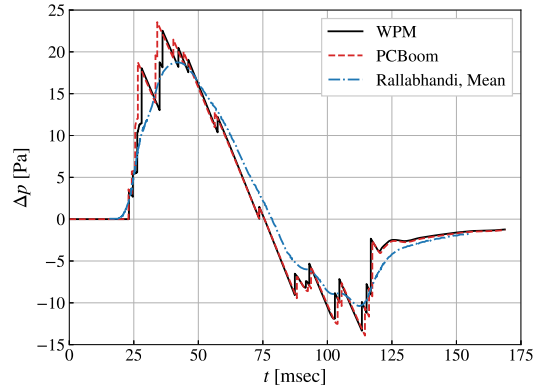
(a) Axisymmetric equivalent area near-field.



(b) Sonic boom through a standard atmosphere.



(c) Sonic boom through atmosphere 3.



(d) Sonic boom through atmosphere 4.

Fig. 5 Sonic boom validation for the axisymmetric equivalent area concept.

$$z_{LE} = Ax^n, \quad (15)$$

$$z_{FS} = Bz^n, \quad (16)$$

and

$$z_{LS} = A \frac{z - x \tan \theta}{\tan \beta - \tan \theta}, \quad (17)$$

where z_{LE} , z_{FS} , and z_{LS} represent the z -coordinates for the leading edge, the freestream surface, and the lower surface, respectively. For this study, we set $A = 0.66$, $n = 0.50$, $\theta = 7.0$ deg., and $\beta = 7.0$ deg. The after-body converges to a cylindrical cross-section at -2.0 deg. from 0.50 to 1.20 m. In the original study of Starkey and Lewis [9], the forebody of the vehicle is 50.0 m long. We scale the geometry by a factor of 10^{-2} with to the original parameters [9]. This scaling is chosen so that the leading geometry is on the same order of magnitude as contemporary waveriders.

C. Grid Independence

A grid independence study for the Sears-Haack [7] geometry is performed. Five radial mesh sizes are considered consisting of: 201, 401, 801, 1101, and 2001 points. Hypersonic near-field studies conducted by King and Miller [6]

showed grid independence with 801 radial grid points for propagation to source cylinder $rL^{-1} = 0.20$. Therefore, a maximum number of 2001 grid points are used for comparison for propagation up to $rL^{-1} = 0.3937$ in the present study. The parabolized solver determines the appropriate number of downstream planes for a solution [4] algorithmically. We limit the maximum streamwise marching step-size to $\Delta x = 0.001$ m to ensure high-fidelity near-field signature resolution.

The stiffest numerical case with the farthest downstream radiating wave in the near-field is chosen for this study. This case corresponds to $M_\infty = 15.0$ with including viscous terms and non-equilibrium reacting flow effects. Freestream static density and temperature are $\rho_\infty = 0.1948$ kg/m³ and $T_\infty = 217.0$ K, respectively. These conditions require the highest grid resolution. Figure 6 shows the near-field waveform of $M_\infty = 15.0$, with viscous, reacting flow over the Sears-Haack geometry. The near-field is extracted at $rL^{-1} = 0.3937$, which is within the acceptable range noted by Loubeau and Coulouvrat [38]. Maximum relative difference in predicted overpressure for the computational grid with 1101 radial grid points is 0.53%. This is acceptable due to a percent difference less than unity. Based on this study, we use 1101 grid points in the the radial direction for all cases examined.

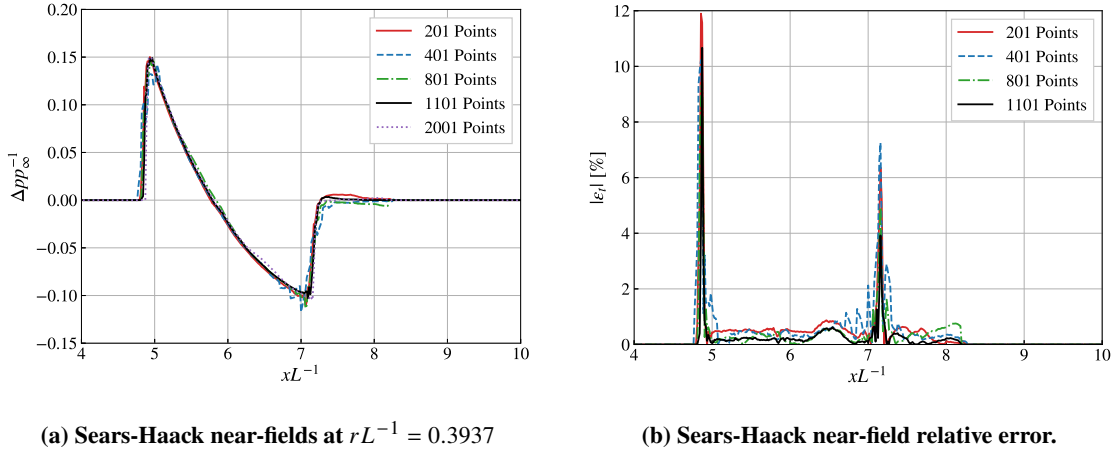
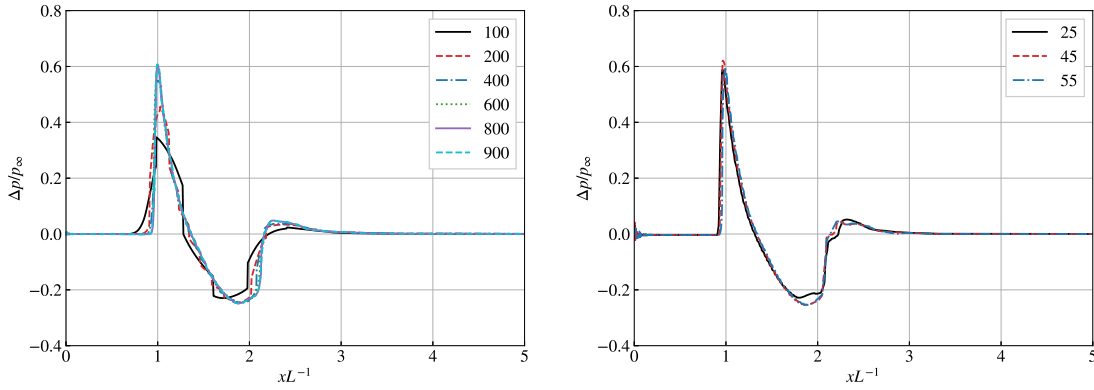


Fig. 6 Grid independence study for Sears-Haack geometry at $M_\infty = 15.0$.

Grid independence studies are also conducted for the two three-dimensional geometries. The freestream Mach number of the HIFiRE-5 vehicle of Juliano et al. [52] is $M_\infty = 7.0$. This M_∞ , along with viscous and reacting flow effects, represents the case where the most grid points are required to resolve the flow-field. Six separate grid sizes are studied, with a number of radial grid points ranging from 100 to 900, as shown in Fig. 7. We find that 901 grid points is more than adequate to resolve the radiating shock wave at a distance $rL^{-1} = 0.20$ from the vehicle centerline. Maximum p_∞ -normalized predicted overpressure is 0.604 for the case with 801 grid points and 0.608 for the case with 901 grid points, a 0.57% difference. Thus, a relative percentage error less than unity relative to the highest density grid shows that 800 radial grid points is acceptable for all cases. Based on this numerical grid independence study, we use 800 grid points in the radial direction for both three-dimensional geometries studied. The maximum difference between the two highest resolutions results in a 1.0% difference in overpressure of the leading bow shock wave in the near-field.

D. Sears-Haack Near-Field and Sonic Boom

Figure 8 shows a numerical schlieren of the Sears-Haack geometry at $M_\infty = 7.0$ with viscous terms enabled. Flow moves from left to right. The contours are dark on the onset of the leading (left) and trailing (right) shock waves. Contours tending to white represent the region of Prandtl-Meyer expansion fans between the leading and trailing shock waves. Within approximately 0.020 m in the cross-stream direction, resides a bright colored region representing the boundary layer. It is within this boundary layer that non-equilibrium real gas effects dominate, which have an effect on the near-field and sonic boom. Figure 9a shows the near-field signature of the Sears-Haack body at $M_\infty = 7.0$. Near-field predictions are presented for inviscid ideal gas, viscous ideal gas, inviscid non-equilibrium gas, and viscous non-equilibrium gas. An apparent difference between each of the predictions is the increase in shock wave overpressure for the viscous cases versus the inviscid cases. For example, freestream normalized overpressure for viscous ideal gas



(a) Near-fields for radial grid independence.

(b) Near-fields for azimuthal grid independence.

Fig. 7 Near-field extraction at $rL^{-1} = 0.20$ for viscous reacting flow at $M_\infty = 6.0$.

and non-equilibrium gas is 0.092 and 0.087, respectively. For inviscid ideal gas and non-equilibrium gas, the predicted overpressures are 0.081 and 0.076, respectively. It is noted that all viscous cases have a larger overpressure than inviscid cases. However, the inclusion of a real non-equilibrium gas model reduces predicted overpressure relative to the ideal gas model by 5.64%, on average for Mach 7.0 flow.

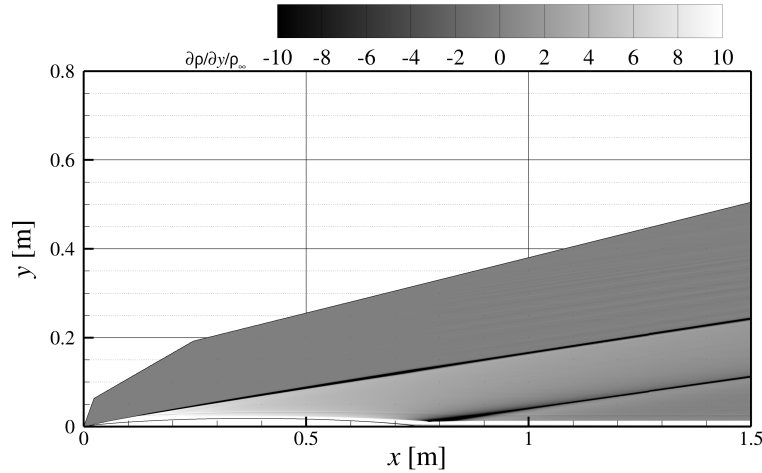


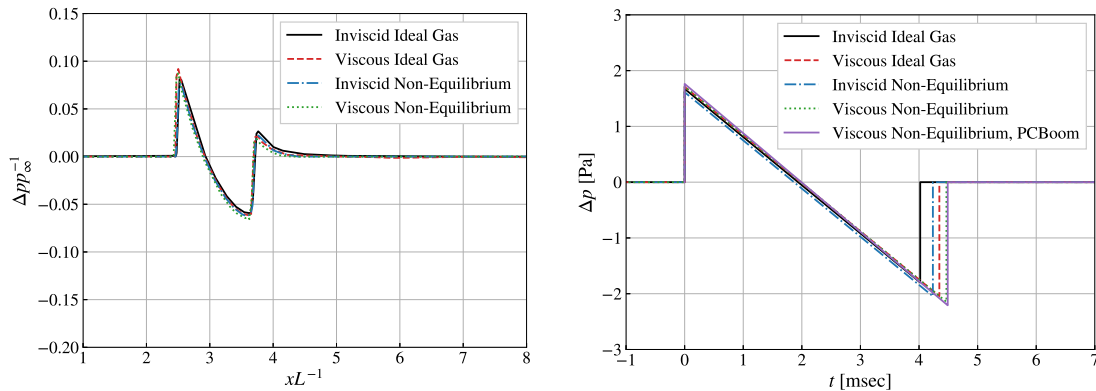
Fig. 8 Numerical schlieren, $\frac{1}{\rho_\infty} \frac{\partial p}{\partial y}$, of Sears-Haack geometry at $M_\infty = 7.0$ for viscous flow.

Predictive capability of WPM for hypersonic M_∞ must be ascertained. Figure 9 shows, side-by-side, hypersonic near-field prediction of the Sears-Haack geometry at $M_\infty = 7.0$ and its sonic boom signature from an altitude of 15.850 km through a quiescent atmosphere. In Figure 9a, and for succeeding near-field predictions in this paper, features flight-vehicle length normalized distance, xL^{-1} on the x -axis and p_∞ -normalized change in static pressure, p , on the y -axis. Inviscid flow prediction is shown as a solid black line, viscous flow prediction is a dashed red line, inviscid non-equilibrium flow is a dashed-dotted blue line, and viscous non-equilibrium flow is a dotted green line.

The Sears-Haack near-field is propagated to the ground through a quiescent, standard atmosphere. The altitude is 15.850 km, and the ground reflection factor is 1.90. Figure 9b shows the sonic boom pressure time history at the ground from the Sears-Haack body at $M_\infty = 7.0$. Similar to the near-field predictions, there is an increase in overpressure at the ground for cases with viscous terms enabled. Particularly, the overpressures at the ground for viscous flow are 1.709 and 1.712 Pa for an ideal gas and non-equilibrium gas, respectively. For inviscid flow, the overpressures are 1.673 and 1.612 Pa for an ideal gas and non-equilibrium gas, respectively. Accounting for non-equilibrium, reacting flow in the near-field results in an increased duration of the sonic boom at the ground, as compared to predictions made with an

ideal gas assumption. On average, the duration of the sonic boom at the ground increases by 4.03% with the inclusion of real gas effects for Mach 7.0 flow.

Corresponding sonic boom signatures at the ground in Fig. 9b use the same line and color convention. However, the x -axis now shows time, t , in ms and the y -axis shows dimensional change in pressure, Δp , in Pa. PCBoom is additionally represented as a solid purple line for viscous, non-equilibrium flow. Maximum overpressure in the sonic boom at the ground for viscous, non-equilibrium flow, predicted by WPM is 1.712 Pa and 1.762 Pa predicted by PCBoom. This is a relative difference to PCBoom of 2.81%. The duration of the sonic boom predicted by WPM is 4.46 ms, and the duration predicted by PCBoom is 4.49 ms. This is a relative difference to PCBoom of 0.49%. Thus, in the hypersonic regime, WPM predicts sonic boom overpressure and duration metrics within 3.0% of PCBoom. This shows acceptable hypersonic sonic boom predictive capability with WPM and can be expanded to other Mach numbers within a larger design space. Due to a lack of experimental data or analytical solution, it is not possible to definitively determine which propagation solver is more accurate for complicated geometries and atmospheres.



(a) Near-field at $M_\infty = 7.0$ and $rL^{-1} = 0.3937$.

(b) Sonic boom at the ground at $M_\infty = 7.0$.

Fig. 9 Hypersonic sonic boom validation of WPM with PCBoom for the Sears-Haack geometry.

1. Prediction of Hypersonic Near-Field and Sonic Boom for an Extended Mach Number Range

We predict the near-field signature and sonic boom of the Sears-Haack geometry for freestream Mach numbers: $M_\infty = 4.0, 5.0, 6.0, 7.0, 7.5, 8.0, 8.5, 9.0, 10.0, 12.0,$ and 15.0 . Atmospheric conditions are $\rho_\infty = 0.1948 \text{ kg/m}^3$ and $T_\infty = 217.0 \text{ K}$. Figures 10 through 12 show Sears-Haack near-field predictions on the left and corresponding sonic boom ground signatures on the right. Solid black lines denote an inviscid ideal gas flow, dashed red lines denote a viscous ideal gas flow, dashed-dotted blue lines denote an inviscid non-equilibrium flow, and dotted green lines indicate a viscous non-equilibrium flow. Trends are extracted for near-field overpressure, sonic boom overpressure, and sonic boom duration. The average, p_∞ normalized, near-field overpressure over the M_∞ range studied is 0.0927 for inviscid flow, 0.1056 for viscous flow, 0.0888 for inviscid reacting flow, and 0.1027 for viscous reacting flow. It is clear that inclusion of the viscous stress tensor is the most influential factor for near-field prediction, which increases predicted overpressure by 13.9% for an ideal gas and 15.7% for a real gas. These trends are apparent in Fig. 13a, which show near-field overpressure normalized as c_p , where $c_p = 2(p - p_\infty)(\gamma p_\infty M_\infty^2)^{-1}$. The dotted lines are exponential equations of best fit. The decrease in maximum c_p as a function of M_∞ shows a log-linear relationship with a rate of -0.158 for inviscid flow, -0.149 for viscous flow, -0.154 for inviscid reacting flow, and -0.144 for viscous reacting flow. The effect of reacting flow is also considered. Across the M_∞ range studied, accounting for real gas and reacting flow effects decreases the near-field predicted overpressure of inviscid and viscous flow by 4.25% and 2.75%, respectively.

The effect of viscosity and non-equilibrium air chemistry influences the characteristics of sonic boom at the ground. For the Sears-Haack geometry, inclusion of viscous effects in the near-field increases the predicted sonic boom overpressure by 7.28% for an ideal gas and 8.49% for a non-equilibrium gas. The inclusion of non-equilibrium air chemistry in the near-field decreases the predicted sonic boom overpressure by 3.01% for inviscid flow and 1.90% for viscous flow. Figure 13b shows sonic boom overpressure at the ground against M_∞ . The importance of viscous terms is apparent with higher hypersonic M_∞ . The discrepancy of predicted overpressure at the ground for $M_\infty = 4.0$ for inviscid and viscous

flow are within 0.10 Pa of each other. This difference triples as M_∞ approaches 15.0. For all cases, including viscous terms increases the predicted sonic boom overpressure at the ground. The reason for viscosity increasing overpressure is explained in King and Miller [6], where the existence of the boundary layer distributes Prandtl-Meyer expansion fans over a greater distance, thus, lowering attenuation of the leading shock wave. A similar trend is observed in the sonic boom duration at the ground. Including viscous terms increases the sonic boom duration at the ground by 7.89% for an ideal gas assumption and 5.22% for a non-equilibrium gas. Overall, these predictions over the range $M_\infty = 4.0$ to 15.0 show that viscosity and non-equilibrium real gas effects must be accounted for in hypersonic flow for the purpose of sonic boom prediction.

We present spectral comparisons for the sonic boom signature of the Sears-Haack geometry at $M_\infty = 6.0, 7.0,$ and 10.0 in Fig. 14. Figure 14a shows SPL for the sonic boom signature of the Sears-Haack geometry at $M_\infty = 6.0$ from an altitude of 15.850 km. The reference pressure is $p_{\text{ref}} = 20.0 \mu\text{Pa}$. The maximum SPL is 82.57 dB at 254.87 Hz for inviscid flow, 82.32 dB at 240.46 Hz for viscous flow, 83.36 dB at 239.96 Hz for non-equilibrium inviscid flow, and 83.90 dB at 230.29 Hz for non-equilibrium viscous flow. Figure 14b shows SPL per unit Hz for the sonic boom signature of the Sears-Haack geometry at $M_\infty = 7.0$. The maximum SPL is 82.93 dB at 248.73 Hz for inviscid flow, 83.95 dB at 230.46 Hz for viscous flow, 83.62 dB at 236.04 Hz for non-equilibrium inviscid flow, and 84.31 dB at 223.83 Hz for non-equilibrium viscous flow. Figure 14c shows SPL per unit Hz for the sonic boom signature of the Sears-Haack geometry at $M_\infty = 10.0$. The maximum SPL is 82.93 dB at 231.93 Hz for inviscid flow, 85.17 dB at 210.73 Hz for viscous flow, 84.34 dB at 224.75 Hz for non-equilibrium inviscid flow, and 85.25 dB at 209.50 Hz for non-equilibrium viscous flow. Overall, the most influential parameter in SPL at the ground is viscosity, increasing peak SPL by 0.78% for $M_\infty = 6.0$, 1.03% for $M_\infty = 7.0$, and 1.28% for $M_\infty = 10.0$. There is a negative frequency shift in peak SPL of approximately 20 Hz for each peak in the sound spectrum due to the lengthening of the sonic boom duration at the ground.

We observe from the predicted hypersonic near-field and sonic boom that viscosity is the most influential factor relative to overpressure. We also note that the difference in inviscid and viscous predictions diverge with an increase in M_∞ . Figure 15 shows numerical schlierens of the Sears-Haack geometry for viscous flow at $M_\infty = 4.0$ and 15.0 , respectively. It is noted that near the surface of the vehicle, the developing laminar boundary layer is much thicker for the $M_\infty = 15.0$ case than the $M_\infty = 4.0$ case. This is also observed in Fig. 16, which shows the velocity profiles extracted at $x = 0.20, 0.40,$ and 0.60 m for both freestream Mach numbers. Predictions and derived quantities are presented dimensionally to illustrate the difference between the two cases. At $x = 0.60$ m, the boundary layer displacement thickness is 0.005 m for $M_\infty = 4.0$ flow and 0.0099 m for $M_\infty = 15.0$ flow. The displacement thickness for $M_\infty = 15.0$ flow is larger than $M_\infty = 4.0$ flow by a factor of approximately 1.9 spanning over the vehicle.

The displacement thickness, $\delta^* = \int_0^\infty (1 - \rho u(\rho_e u_e)^{-1}) dy$, grows with s_l , where s_l is the streamwise position measured on the surface from the leading edge. If $M_\infty \gg 1$ and $M_\infty d\delta^*/ds_l \ll 1$, then the boundary layer edge pressure ratio, p_e/p_∞ , becomes

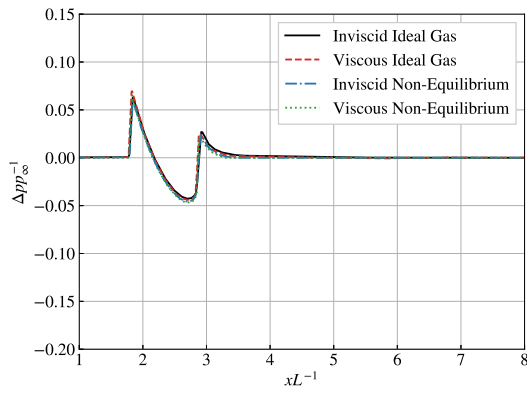
$$\frac{p_e}{p_\infty} = 1 + \gamma M_\infty \frac{d\delta^*}{ds_l} + \frac{\gamma(\gamma + 1)}{4} \left(M_\infty \frac{d\delta^*}{ds_l} \right)^2. \quad (18)$$

It is readily apparent that the edge pressure, p_e , is dependent on δ^* with increasing distance, s_l . It is also apparent that p_e goes as M_∞^2 . This explains the divergence of near-field and sonic boom overpressure. Between viscous and inviscid flows, $\Delta p p_\infty^{-1}$ increases with M_∞ because δ^* increases with M_∞ and the Prandtl-Meyer expansion fan becomes distributed over the boundary layer. Attenuation of the leading shock wave is reduced, and this causes an increase in predicted overpressure with increasing M_∞ , as well as a decrease in trailing shock strength with increasing M_∞ .

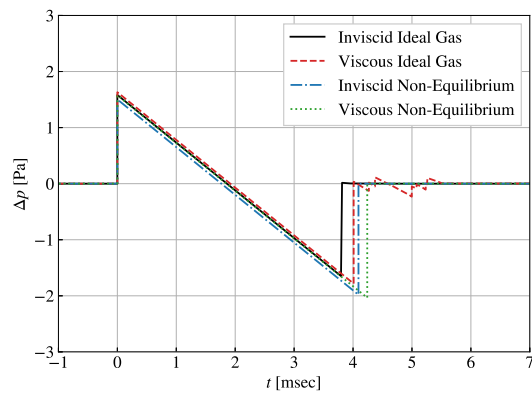
E. HIFiRE-5 Near-Field and Sonic Boom Prediction

The HIFiRE-5 geometry was partly created to support studies of three-dimensional aerothermodynamics and transition to turbulence. We predict the flow-field of the HIFiRE-5 hypersonic test vehicle for $M_\infty = 5.0, 6.0,$ and 7.0 . The atmospheric conditions in each case are $\rho_\infty = 0.1948 \text{ kg/m}^3$ and $T_\infty = 217.0 \text{ K}$. Sonic boom is propagated from an altitude of 15.850 km through a quiescent standard atmosphere. We focus on predictions that include viscous effects, similar to the study by Juliano et al. [52].

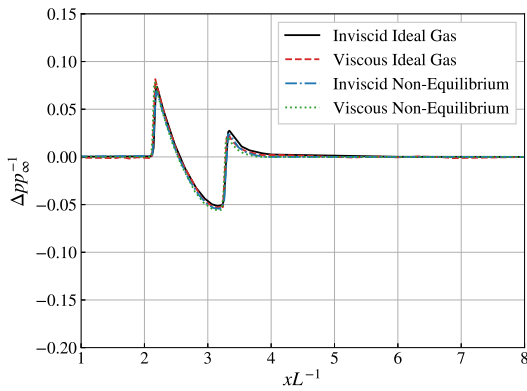
Figure 17 shows contour slices of p_∞ -normalized change in pressure, Δp , at four downstream locations: $x = 0.50, 0.75, 1.25,$ and 1.50 m. Light blue color represents the freestream condition when $\Delta p p_\infty^{-1} = 0.0$. Contours are white for values $\Delta p p_\infty^{-1} < 0.050$. Maximum pressure occurs when the azimuthal angle approaches the sideline, $\phi = 90.0$ deg. This is presented as the white region.



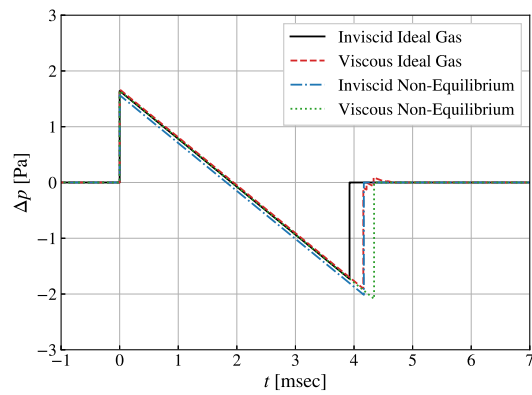
(a) Near-field at $M_\infty = 5.0$ and $rL^{-1} = 0.3937$.



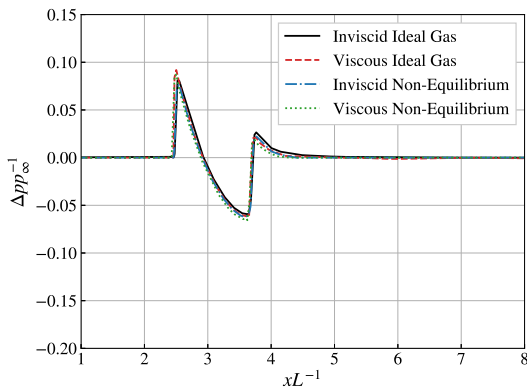
(b) Sonic boom at the ground at $M_\infty = 5.0$.



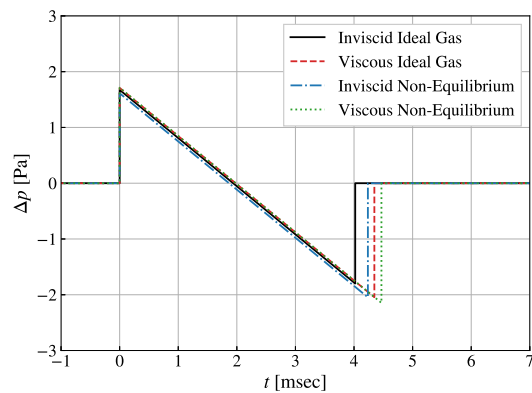
(c) Near-field at $M_\infty = 6.0$ and $rL^{-1} = 0.3937$.



(d) Sonic boom at the ground at $M_\infty = 6.0$.

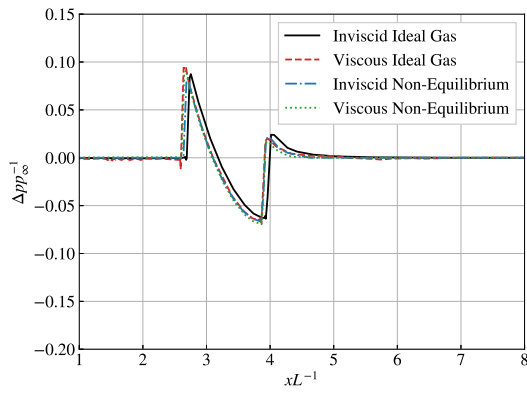


(e) Near-field at $M_\infty = 7.0$ and $rL^{-1} = 0.3937$.

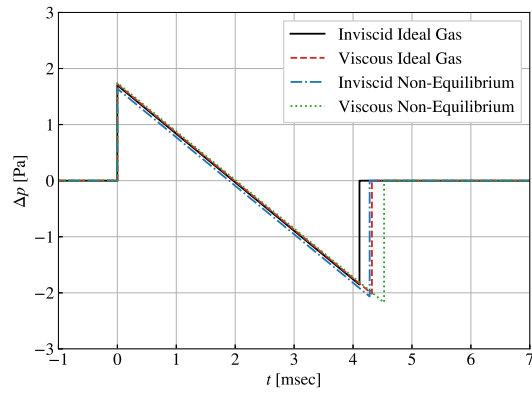


(f) Sonic boom at the ground at $M_\infty = 7.0$.

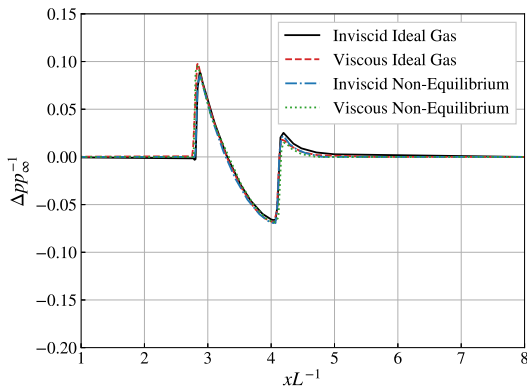
Fig. 10 Near-field predictions (left) and sonic boom predictions (right) for the Sears-Haack geometry.



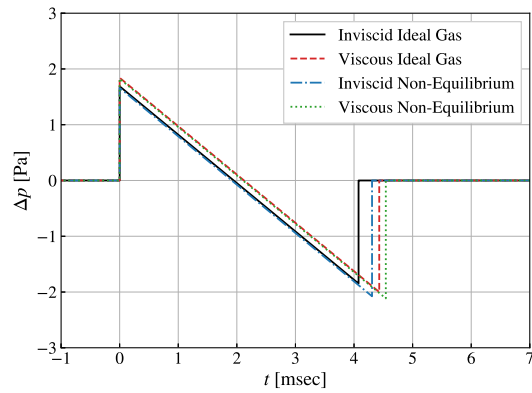
(a) Near-field at $M_\infty = 7.5$ and $rL^{-1} = 0.3937$.



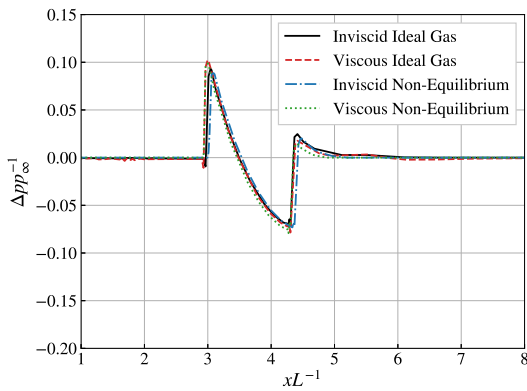
(b) Sonic boom at the ground at $M_\infty = 7.5$.



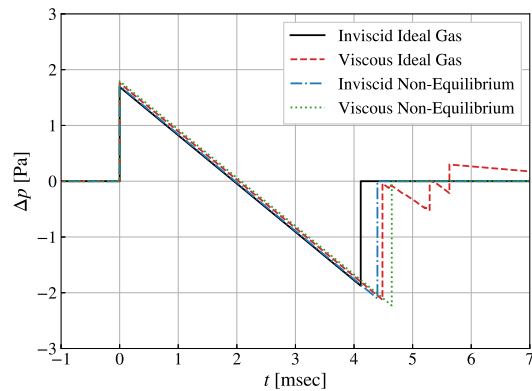
(c) Near-field at $M_\infty = 8.0$ and $rL^{-1} = 0.3937$.



(d) Sonic boom at the ground at $M_\infty = 8.0$.

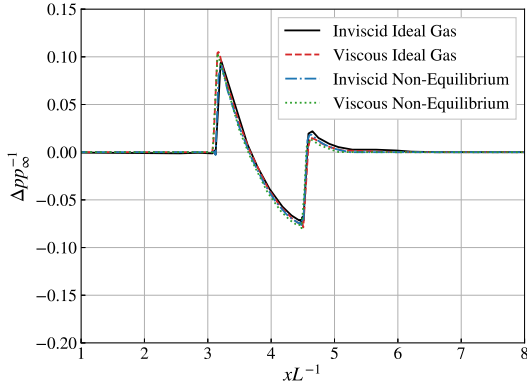


(e) Near-field at $M_\infty = 8.5$ and $rL^{-1} = 0.3937$.

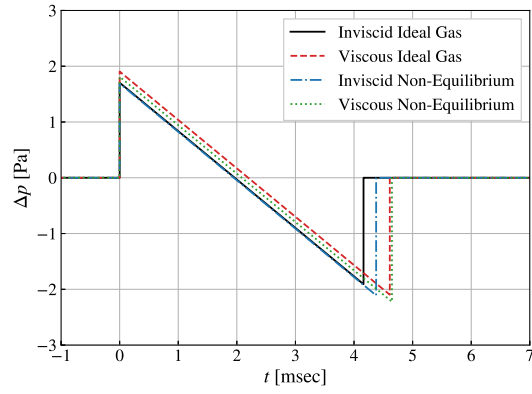


(f) Sonic boom at the ground at $M_\infty = 8.5$.

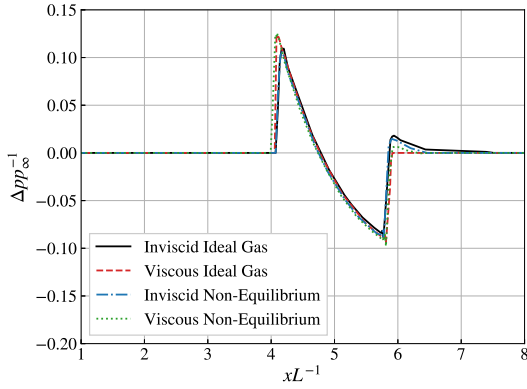
Fig. 11 Near-field predictions (left) and sonic boom predictions (right) for the Sears-Haack geometry.



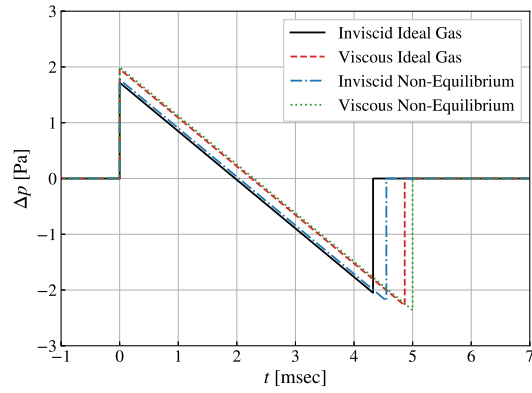
(a) Near-field at $M_\infty = 9.0$ and $rL^{-1} = 0.3937$.



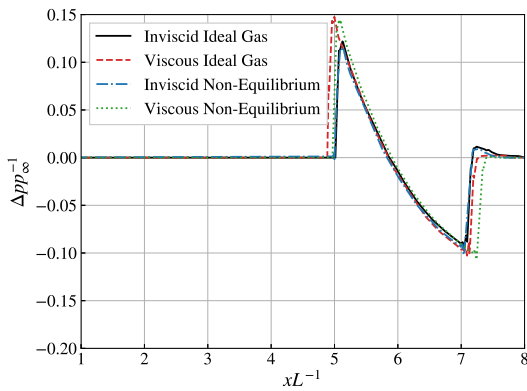
(b) Sonic boom at the ground at $M_\infty = 9.0$.



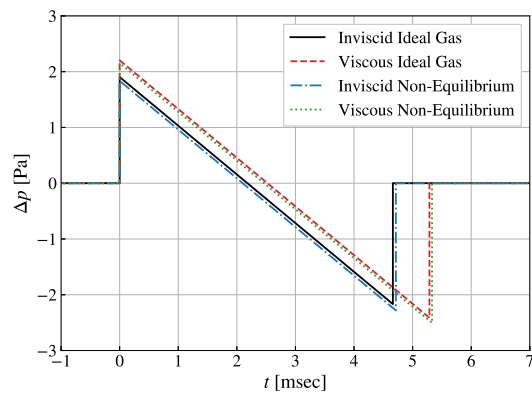
(c) Near-field at $M_\infty = 12.0$ and $rL^{-1} = 0.3937$.



(d) Sonic boom at the ground at $M_\infty = 12.0$.

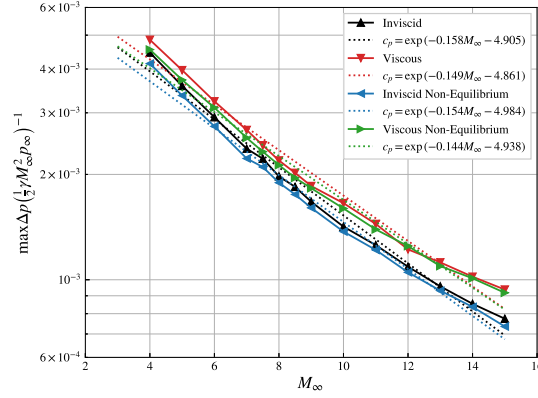


(e) Near-field at $M_\infty = 15.0$ and $rL^{-1} = 0.3937$.

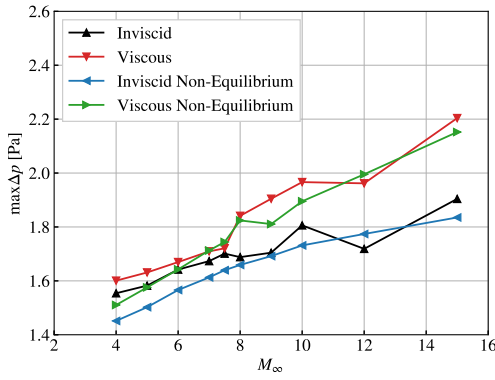


(f) Sonic boom at the ground at $M_\infty = 15.0$.

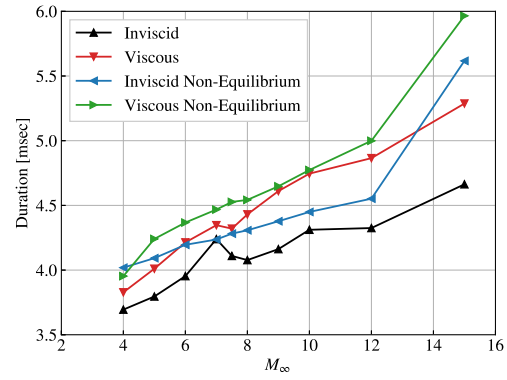
Fig. 12 Near-field predictions (left) and sonic boom predictions (right) for the Sears-Haack geometry.



(a) Near-field overpressures.



(b) Sonic boom overpressures.



(c) Sonic boom durations for the Sears-Haack geometry.

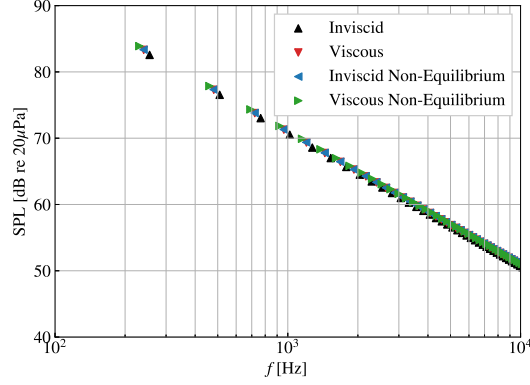
Fig. 13 Hypersonic near-field ($rL^{-1} = 0.3937$) and sonic boom trends for the Sears-Haack geometry.

For inviscid and non-equilibrium flow at $M_\infty = 5.0$, near-field, p_∞ -normalized predicted overpressure is 0.508 and 0.496, respectively. Assuming an ideal gas, there is an increased relative difference in overpressure by 2.36%. For $M_\infty = 6.0$ flow, the predicted overpressures is 0.551 and 0.554, respectively, which is a 0.54% relative difference. At $M_\infty = 7.0$ flow, predicted overpressure is 0.605 and 0.583, respectively. This is a relative difference of 3.64%.

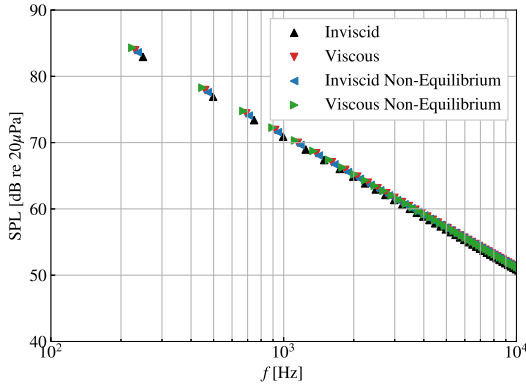
Near-field signatures are propagated to the ground to predict sonic boom. For inviscid and non-equilibrium flow at $M_\infty = 5.0$, sonic boom predicted overpressure is 9.951 and 9.947 Pa, respectively. Assuming an ideal gas, there is a decrease in relative overpressure of 0.04%. At $M_\infty = 6.0$, predicted overpressures are 10.07 and 10.03 Pa, respectively. This is a relative difference of 0.40%. At $M_\infty = 7.0$, predicted overpressures are 10.80 and 10.73 Pa, respectively. This is a relative difference of 0.65%. Overall, the relative differences in near-field overpressure between an ideal gas flow and a non-equilibrium flow decrease as the waves propagate to the ground. For instance, at $M_\infty = 5.0$, an initial relative difference of 2.96% in near-field overpressure decreases to 0.42% at the ground.

Although the relative difference between predicted overpressure for an ideal gas and a non-equilibrium gas are smaller than one percent at the ground, there are noticeable differences in the ground spectra. The main differences in ground signature are shown in Figs. 18b, 18d, and 18f, where the duration is longer for non-equilibrium cases. For example, for $M_\infty = 7.0$ of Fig. 18f, the sonic boom duration for the ideal gas case is 9.91 ms. The duration for the non-equilibrium case is 10.3 ms, which is a 3.9% difference. The increase in sonic boom duration has an effect on the ground spectra. Figure 22 shows the SPL at the ground for each predicted sonic boom signature. For the same case at $M_\infty = 7.0$, peak SPL is 92.42 dB at 91.5 Hz for inviscid flow and 94.82 dB at 69.3 Hz. The sonic boom duration increases by 3.9% for non-equilibrium flow and decreases the peak SPL frequency by 24.3%.

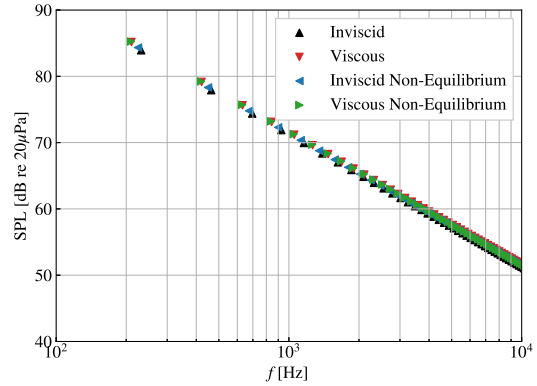
We make predictions of the hypersonic near-field and sonic boom signature at the ground for real gas and non-equilibrium reacting flows. The hypersonic near-field is extracted at $rL^{-1} = 0.20$. Figures 18a, 18c, and 18e show



(a) $M_\infty = 6.0$.



(b) $M_\infty = 7.0$.



(c) $M_\infty = 10.0$.

Fig. 14 SPL of the Sears-Haack sonic boom signature.

these near-field predictions. Unlike predictions made for the Sears-Haack geometry in Figs. 10 through 12, including non-equilibrium reacting effects does not have an apparent effect on near-field prediction. Maximum relative error occurs with maximum overpressure for $M_\infty = 7.0$ in Fig. 18e, which is approximately 3.6%.

However, the effects of non-equilibrium reacting flow have a significant effect on the sonic boom at the ground. Figures 18b, 18d, and 18f show the sonic boom ground signature for the HIFIRE-5 at $M_\infty = 5.0, 6.0,$ and 7.0 . Ideal gas predictions are shown as a solid red line, and non-equilibrium flow are shown as a dashed blue line. The main differences in the sonic boom signature at the ground are seen in Figs. 21b, 21d, and 21f, where the duration is often longer for the non-equilibrium cases. For example, for $M_\infty = 7.0$ flow in Fig. 21f, the sonic boom duration for the ideal gas case is 25.4 ms, and the duration for the non-equilibrium case is 25.8 ms. This represents a 1.6% relative difference. The increase in sonic boom duration has an effect on the SPL. This is shown in Fig. 19, where there is a negative shift in the frequency of peak SPL. For the same case at $M_\infty = 7.0$, peak SPL is 88.58 dB at 39.6 Hz for an ideal gas and 102.40 dB at 39.5 Hz. The sonic boom duration increases by 1.6% for non-equilibrium flow and decreases the peak SPL frequency by 0.25%.

F. Power-Law Waverider Near-Field and Sonic Boom Prediction

We apply this combined parabolized approach to $M_\infty = 5.0, 6.0,$ and 7.0 for the power-law waverider. The atmospheric conditions at each M_∞ are $\rho_\infty = 0.1948 \text{ kg/m}^3$, $T_\infty = 217.0 \text{ K}$, and are quiescent. The flight-vehicle altitude is 15.850 km. The flow-field of the waverider at $M_\infty = 7.0$ is shown in Fig. 20, with x -axis slices extracted at streamwise locations of $x = 0.20, 0.30,$ and 0.40 m . Light blue contours represent regions of the flow-field, where local static pressure matches global freestream pressure. Contour colors approach orange when there is an increase in pressure. Static pressure decreases in the streamwise direction on the surface.

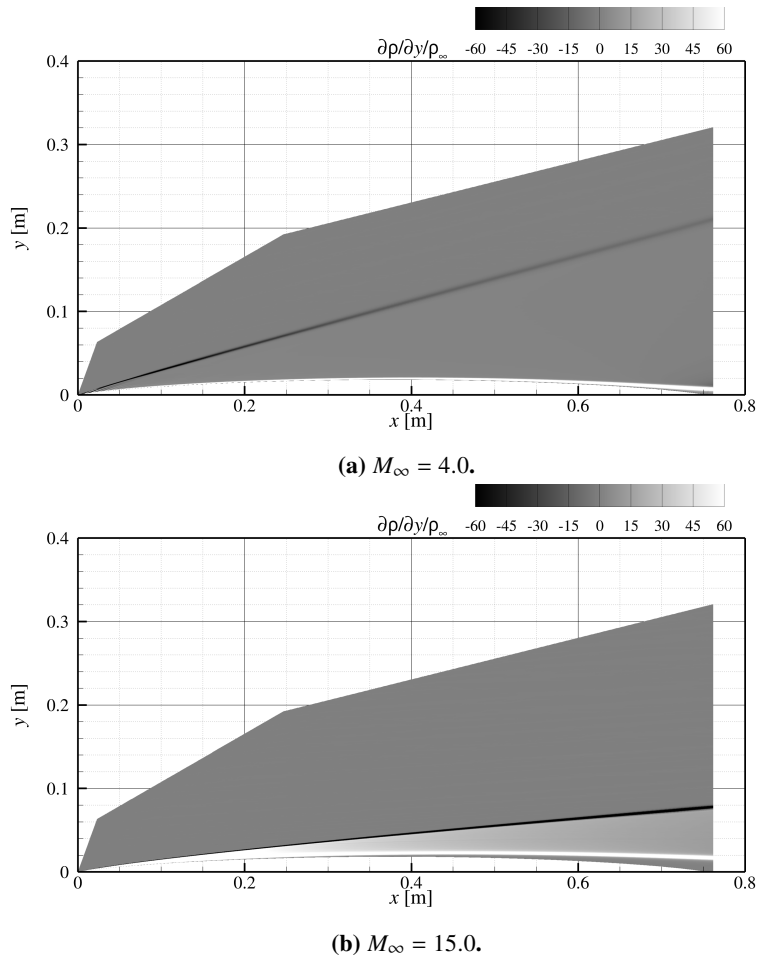


Fig. 15 Numerical schlieren, $\frac{1}{\rho_\infty} \frac{\partial \rho}{\partial y}$, of Sears-Haack geometry at $M_\infty = 4.0$ (top) and $M_\infty = 15.0$ (bottom).

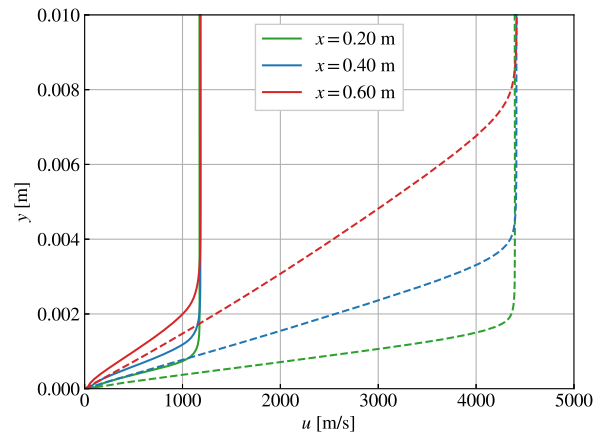


Fig. 16 Boundary layer velocity profiles of the Sears-Haack geometry at $M_\infty = 4.0$ (solid lines) and $M_\infty = 15.0$ (dashed lines).

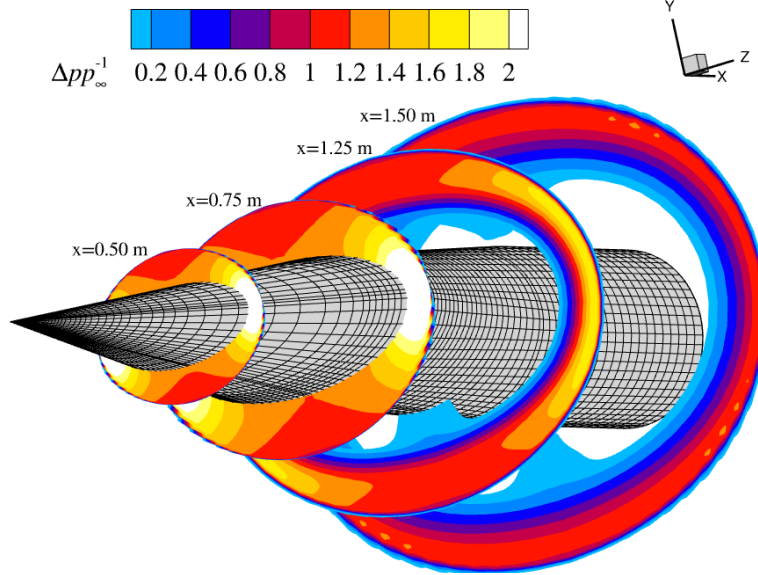


Fig. 17 Contours of p_∞ -normalized change in static pressure for the HIFiRE-5 geometry at $M_\infty = 6.0$ for inviscid flow.

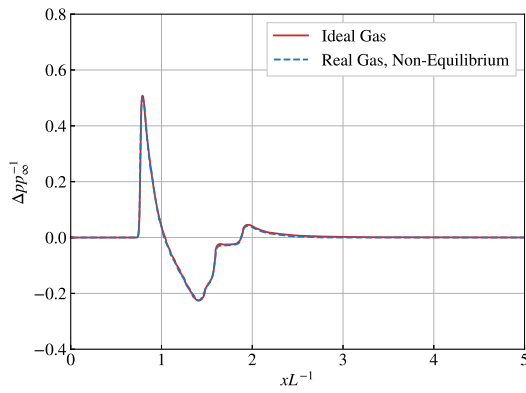
For inviscid and non-equilibrium flow at $M_\infty = 5.0$, near-field p_∞ -normalized predicted overpressure of 0.452 and 0.439, respectively. Assuming an ideal gas, there is an increased relative difference in overpressure by 2.96%. At $M_\infty = 6.0$, the predicted overpressures become 0.596 and 0.652, respectively, which is a 9.45% relative difference. At $M_\infty = 7.0$, predicted overpressure becomes 0.811 and 0.757, respectively. This is a relative difference of 6.6%.

The near-field signatures are propagated to the ground to compute the sonic boom. For an ideal gas and non-equilibrium flow at $M_\infty = 5.0$, sonic boom predicted overpressure is 4.37 and 4.39 Pa, respectively. Assuming an ideal gas, there is a decreased relative difference in overpressure by 0.42%. For $M_\infty = 6.0$, the predicted overpressures become 4.75 and 4.60 Pa for ideal gas and non-equilibrium, respectively. At $M_\infty = 7.0$ flow, predicted overpressure is 4.83 and 4.81 Pa, respectively. This is a relative difference of 0.47%. Overall, the relative differences in near-field overpressure between an ideal gas flow and a non-equilibrium flow decrease as the sonic boom propagates to the ground. For instance, at $M_\infty = 5.0$, an initial relative difference of 2.96% in near-field overpressure decreases to 0.42% at the ground.

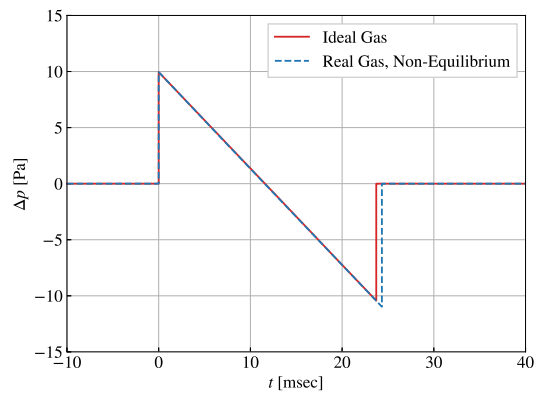
Although the relative difference between predicted overpressures for an ideal gas and a non-equilibrium gas are smaller than one percent at the ground, there is a noticeable difference in the spectra at the ground. Important differences in ground signature are observed in Fig. 21, where the duration is larger for the non-equilibrium cases. For example, at $M_\infty = 7.0$ in Fig. 21f, the sonic boom duration for the ideal gas case is 9.91 ms, and the duration for the non-equilibrium case is 10.3 ms. This is a 3.9% relative difference. The increase in sonic boom duration has an effect on the ground spectra. Figure 22 shows SPL per unit Hz at the ground for each predicted sonic boom signature. For the same case at $M_\infty = 7.0$, peak SPL is 92.42 dB at 91.5 Hz for inviscid flow and 94.82 at 69.3 Hz. The sonic boom duration increases by 3.9% for non-equilibrium flow and decreases the peak SPL frequency by 24.3%.

IV. Conclusion

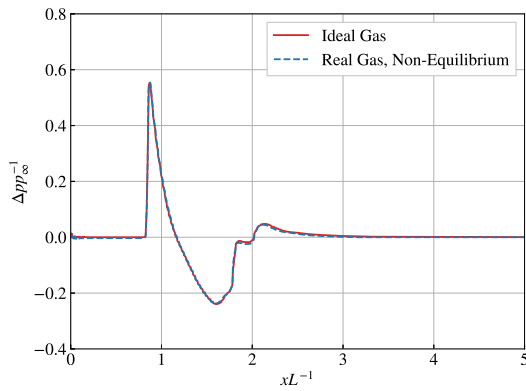
We present a fully-parabolized prediction approach for the hypersonic near-field and sonic boom. The entire method is unique in that the flow-field is marched from the vehicle surface to the ground observer. The near-field is predicted via spatially marching the PNS equations using a modified form of the UPS code of Lawrence et al. [4]. The iterative approach of Miller et al. [42] is employed for regions of flow with upstream influence. The sonic boom ground signature is predicted via propagating the near-field pressure to the ground using WPM [5]. We validate WPM by comparing predictions with PCBoom [19] and publicly available data [49]. Sonic boom predictions using WPM for the axisymmetric equivalent area and LM1021 configurations are within 6.0% of PCBoom and 5.7% of the mean predictions from the Second AIAA/NASA Sonic Boom Prediction Workshop. Including viscous effects for non-equilibrium reacting



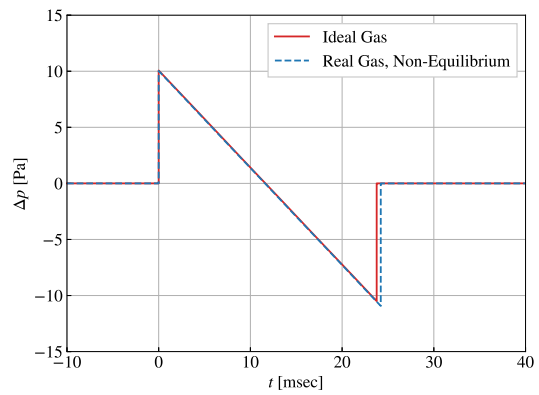
(a) Near-field at $M_\infty = 5.0$ and $rL^{-1} = 0.20$.



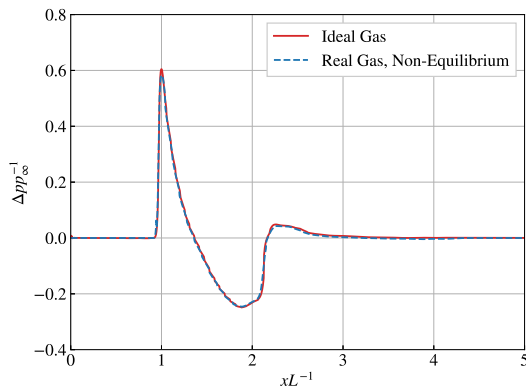
(b) Sonic boom at the ground at $M_\infty = 5.0$.



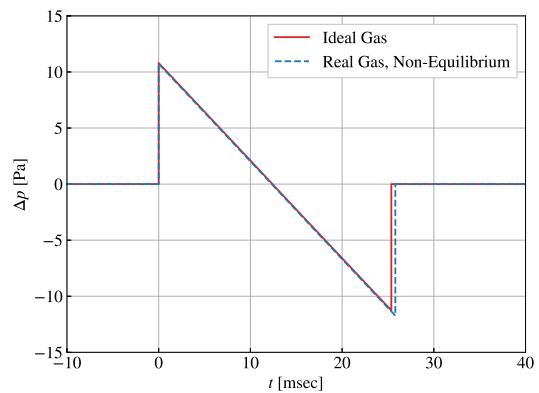
(c) Near-field at $M_\infty = 5.0$ and $rL^{-1} = 0.20$.



(d) Sonic boom at the ground at $M_\infty = 6.0$.



(e) Near-field at $M_\infty = 7.0$ and $rL^{-1} = 0.20$.



(f) Sonic boom at the ground at $M_\infty = 7.0$.

Fig. 18 Near-field predictions (left) and sonic boom predictions (right) for HIFiRE-5 geometry.

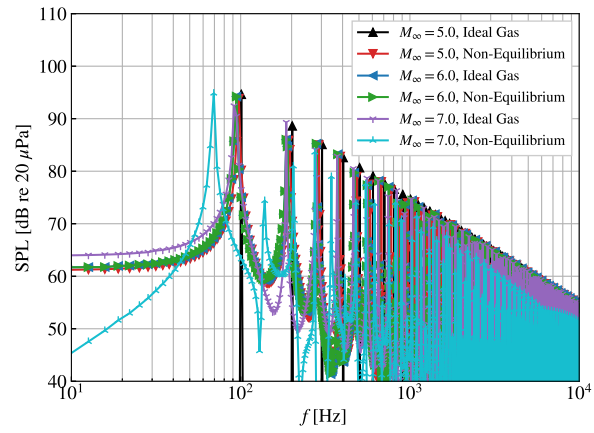


Fig. 19 SPL of the HIFiRE-5 sonic boom signature.

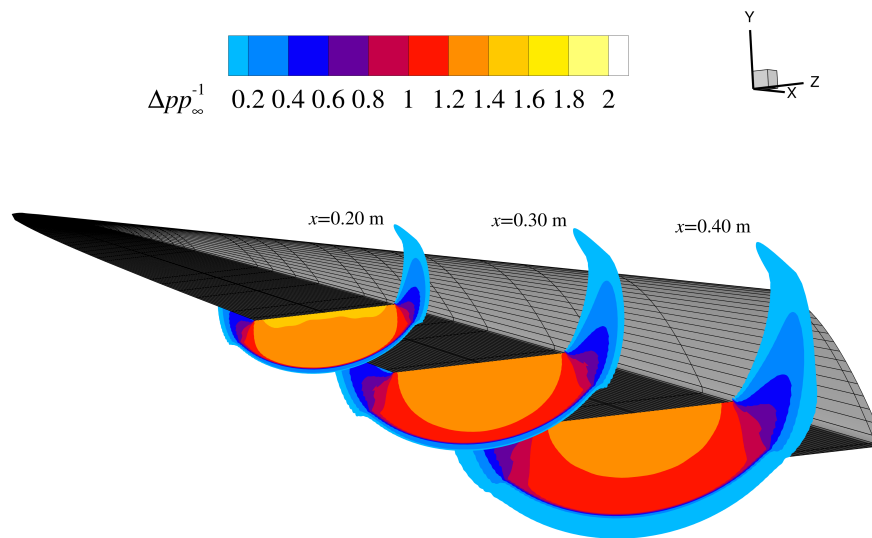
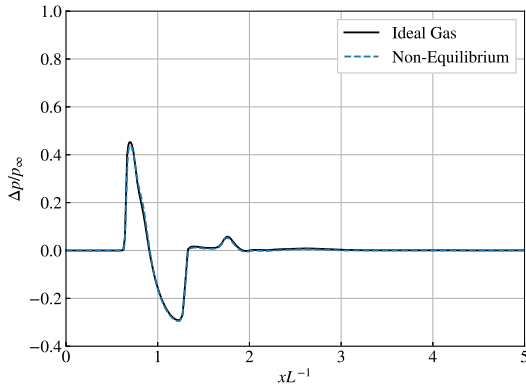
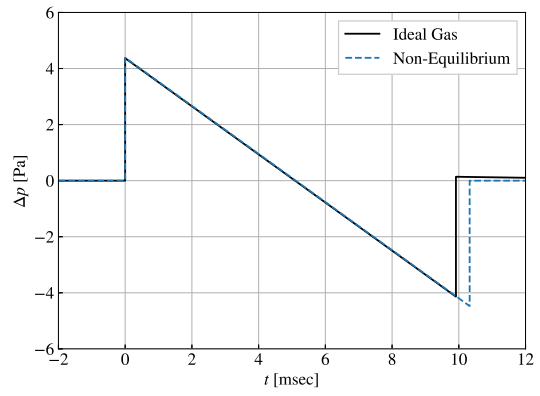


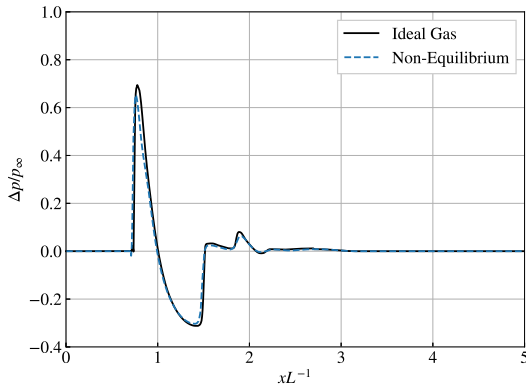
Fig. 20 Contours of p_∞ -normalized change in static pressure for the power-law waverider at $M_\infty = 7.0$ for inviscid flow.



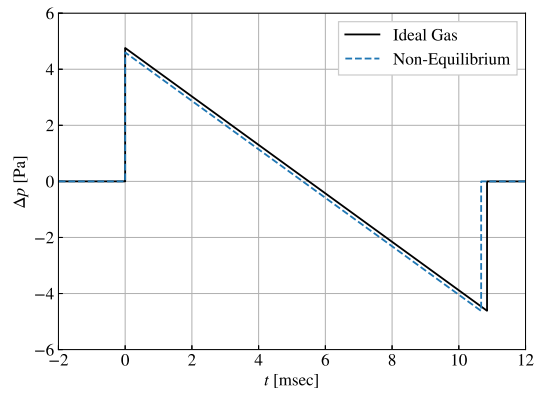
(a) Near-field at $M_\infty = 5.0$ and $rL^{-1} = 0.167$.



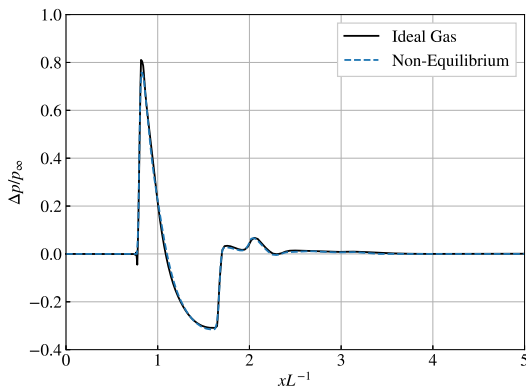
(b) Sonic boom at the ground at $M_\infty = 5.0$.



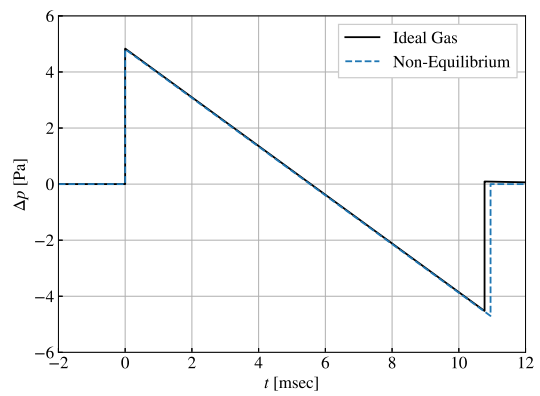
(c) Near-field at $M_\infty = 6.0$ and $rL^{-1} = 0.167$.



(d) Sonic boom at the ground at $M_\infty = 6.0$.



(e) Near-field at $M_\infty = 7.0$ and $rL^{-1} = 0.167$.



(f) Sonic boom at the ground at $M_\infty = 7.0$.

Fig. 21 Near-field predictions (left) and sonic boom predictions (right) for power-law waverider.

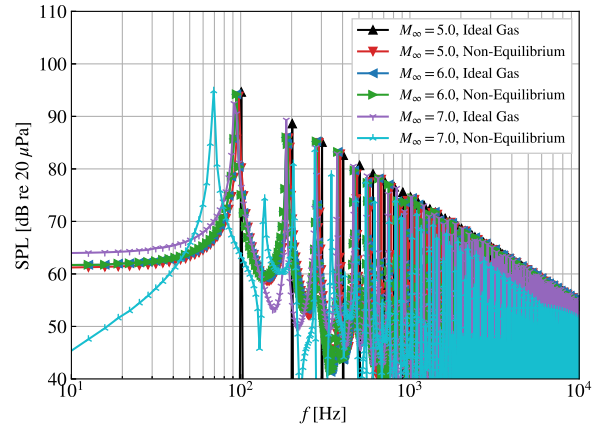


Fig. 22 SPL of the power-law waverider sonic boom signature.

flow increased predicted overpressure in the near-field and sonic boom overpressure by 15.7% and 8.49% on average, respectively. Accounting for non-equilibrium reacting effects decreases predicted overpressure by 1.90%, on average, for viscous flow versus inviscid flow. However, accounting for non-equilibrium, reacting flow increases sonic boom duration by 5.22% compared to an ideal gas flow on average.

We have shown the necessity for including the viscous stress tensor in the prediction of hypersonic sonic boom, which is not essential for supersonic flow [3]. The boundary layer gives rise to a larger distribution of sources of the Prandtl-Meyer expansion waves. This distribution leads to lowered attenuation of the leading shock wave, increasing sonic boom overpressure, and decreases strength of the trailing shock wave. In the future, we will examine a larger design space for waveriders and connect their geometry to the sonic boom foot print.

Acknowledgements

Research was sponsored by the Defense Advanced Research Project Agency (DARPA) and the Army Research Office and was accomplished under Grant Number W911NF-21-1-0342. The views and conclusions contained in this document are those of the authors and should not be interpreted as representing the official policies, either expressed or implied, of the Army Research Office or the U.S. Government. The U.S. Government is authorized to reproduce and distribute reprints for Government purposes notwithstanding any copyright notation herein.

References

- [1] Silva, W. A., Sanetrik, M. D., and Chwalowski, P., "Using FUN3D for aeroelastic, Sonic Boom, and Aeropropulsoservoelastic (APSE) Analyses of a Supersonic Configuration," *15th Dynamics Specialists Conference, AIAA Paper 2016-1319*, 2016. doi:10.2514/6.2016-1319.
- [2] Park, M. A., "Adjoint-Based, Three-Dimensional Error Prediction and Grid Adaptation," *AIAA Journal*, Vol. 42, No. 9, 2004, pp. 1854–1862. doi:10.2514/1.10051.
- [3] Park, M., "Low Boom Configuration Analysis with FUN3D Adjoint Simulation Framework (Invited)," *29th AIAA Applied Aerodynamics Conference, AIAA Paper 2011-3337*, 2011. doi:10.2514/6.2011-3337.
- [4] Lawrence, S. L., Tannehill, J. C., and Chausee, D. S., "Upwind Algorithm for the Parabolized Navier-Stokes Equations," *AIAA Journal*, Vol. 27, No. 9, 1989, pp. 1175–1183. doi:10.2514/3.10243.
- [5] Thomas, C. L., "Extrapolation of Sonic Boom Pressure Signatures by the Waveform Parameter Method," *NASA TN D-6832*, 1972.
- [6] King, C. B., and Miller, S. A. E., "Fully Parabolic Prediction of the Hypersonic Near-Field About Slender Axisymmetric Bodies," *AIAA SCITECH 2023 Forum, AIAA Paper 2023-1424*, 2023. doi:10.2514/6.2023-1424.
- [7] Sears, W. R., "On Projectiles of Minimum Wave Drag," *Quarterly of Applied Mathematics*, Vol. 4, No. 4, 1947, pp. 361–366.

- [8] Kimmel, R., Adamczak, D., Berger, K., and Choudhari, M., “HIFiRE-5 Flight Vehicle Design,” *40th Fluid Dynamics Conference and Exhibit, AIAA Paper 2010-4985*, American Institute of Aeronautics and Astronautics, 2010. doi:10.2514/6.2010-4985, URL <https://doi.org/10.2514/6.2010-4985>.
- [9] Starkey, R. P., and Lewis, M. J., “Critical Design Issues for Airbreathing Hypersonic Waverider Missiles,” *Journal of Spacecraft and Rockets*, Vol. 38, No. 4, 2001, pp. 510–519. doi:10.2514/2.3734.
- [10] Whitham, G. B., “The Flow Pattern of a Supersonic Projectile,” *Communications on Pure and Applied Mathematics*, Vol. 5, No. 3, 1952, pp. 301–348. doi:10.1002/cpa.3160050305.
- [11] Whitham, G. B., “On the Propagation of Weak Shock Waves,” *Journal of Fluid Mechanics*, Vol. 1, No. 3, 1956, pp. 290–318. doi:10.1017/s0022112056000172.
- [12] Carlson, H., *Correlation of Sonic-Boom Theory with Wind-tunnel and Flight Measurements*, NASA-TR-R-213, 1964.
- [13] Whitcomb, R. T., and Fischetti, T. L., “Development of a Supersonic Area Rule and an Application to the Design of a Wing-Body Combination Having High Lift-to-Drag Ratios,” *NACA Research Memorandum L53H31a (Unclassified 1958)*, 1956.
- [14] Whitcomb, R. T., “Some Considerations Regarding the Application of the Supersonic Area Rule to the Design of Airplane Fuselages,” *NACA Research Memorandum 56E23a (Unclassified 1966)*, 1956.
- [15] Hayes, W. D., “Linearized Supersonic Flow,” *Ph.D. Dissertation, California Institute of Technology*, 1947. doi:10.7907/D7N0-4412.
- [16] Hayes, W. D., and Runyan, H. L., “Sonic-Boom Propagation through a Stratified Atmosphere,” *The Journal of the Acoustical Society of America*, Vol. 51, No. 2C, 1972, pp. 695–701. doi:10.1121/1.1912903.
- [17] Seebass, A., “Hypersonic Boom,” *Boeing Scientific Research Laboratories Technical Communication, Vol. 30*, 1970.
- [18] Tiegerman, B., “Sonic Booms of Drag Dominated Hypersonic Vehicles,” *Ph.D. Dissertation, Cornell University*, 1975.
- [19] Plotkin, K., “Review of Sonic Boom Theory,” *12th Aeroacoustic Conference, AIAA Paper 1989-1105*, 1989. doi:10.2514/6.1989-1105.
- [20] Housman, J. A., Kenway, G. K., Jensen, J. C., and Kiris, C. C., “Efficient Near-Field to Mid-Field Sonic Boom Propagation Using a High-Order Space Marching Method,” *AIAA Aviation 2019 Forum*, 2019, p. 3487. doi:10.2514/6.2019-3487.
- [21] Carlson, H., “Simplified Sonic Boom Prediction,” *NASA Technical Paper 1122*, 1978.
- [22] Cramer, M. S., “The Problems that Arise in the Generation and Propagation of Sonic Booms: 1. Flow Fields in the Plane of Symmetry Below a Delta Wing; 2. Focusing of an Acoustic Pulse at an Arete,” *Ph.D. Dissertation, Cornell University*, 1976.
- [23] Morris, O. A., Lamb, M., and Carlson, H. W., *Sonic-Boom Characteristics in the Extreme Near Field of a Complex Airplane Model at Mach Numbers of 1.5, 1.8, and 2.5*, National Aeronautics and Space Administration, NASA-TN-D-5755, 1970.
- [24] Hunton, L. W., “Current Research in Sonic Boom,” *NASA SP-180*, 1968, pp. 57–66.
- [25] Miller, S. A. E., “Alternative Analytical Solution for Planar Oblique Shock Waves,” *American Physical Society Division of Fluid Dynamics*, 2022.
- [26] Jiang, Z., and Yu, H., “Theories and Technologies for Duplicating Hypersonic Flight Conditions for Ground Testing,” *National Science Review*, Vol. 4, No. 3, 2017, pp. 290–296. doi:10.1093/nsr/nwx007.
- [27] Bertin, J. J., and Cummings, R. M., “Critical Hypersonic Aerothermodynamic Phenomena,” *Annual Review of Fluid Mechanics*, Vol. 38, No. 1, 2006, pp. 129–157. doi:10.1146/annurev.fluid.38.050304.092041.
- [28] Bertin, J., *Hypersonic Aerothermodynamics*, AIAA Textbooks Series, AIAA, 1994. doi:10.2514/4.470363.
- [29] Lockman, W. K., Lawrence, S. L., and Cleary, J. W., “Flow Over an All-Body Hypersonic Aircraft-Experiment and Computation,” *Journal of Spacecraft and Rockets*, Vol. 29, No. 1, 1992, pp. 7–15. doi:10.2514/3.26308.
- [30] Morgenstern, J., “How to Accurately Measure Low Sonic Boom or Model Surface Pressure in Supersonic Wind Tunnels,” *30th AIAA Applied Aerodynamics Conference, AIAA Paper 2012-3215*, 2012. doi:10.2514/6.2012-3215.
- [31] Carlson, H. W., and Morris, O. A., “Wind-Tunnel Sonic-Boom Testing Techniques,” *Journal of Aircraft*, Vol. 4, No. 3, 1967, pp. 245–249. doi:10.2514/3.43827.

- [32] Cheung, S. H., Edwards, T. A., and Lawrence, S. L., “Application of Computational Fluid Dynamics to Sonic Boom Near- and Mid-Field Prediction,” *Journal of Aircraft*, Vol. 29, No. 5, 1992, pp. 920–926. doi:10.2514/3.46263.
- [33] Haering, E., Murray, J., Purifoy, D., Graham, D., Meredith, K., Ashburn, C., and Stucky, M., “Airborne Shaped Sonic Boom Demonstration Pressure Measurements with Computational Fluid Dynamics Comparisons,” *43rd AIAA Aerospace Sciences Meeting and Exhibit, AIAA Paper 2005-9*, 2005. doi:10.2514/6.2005-9.
- [34] Luquet, D., Marchiano, R., Coulouvrat, F., Din, I. S. E., and Loseille, A., “Sonic Boom Assessment of a Hypersonic Transport Vehicle with Advanced Numerical Methods,” *21st AIAA/CEAS Aeroacoustics Conference*, American Institute of Aeronautics and Astronautics, AIAA Paper 2015-2685, 2015. doi:10.2514/6.2015-2685.
- [35] Park, M. A., and Carter, M. B., “Low-Boom Demonstrator Near-Field Summary for the Third AIAA Sonic Boom Prediction Workshop,” *Journal of Aircraft*, Vol. 59, No. 3, 2022, pp. 563–577. doi:10.2514/1.c036323.
- [36] Rallabhandi, S., “Focus Boom Simulations Using sBOOM and Lossy Nonlinear Tricomi Equation Solvers,” *The Journal of the Acoustical Society of America*, Vol. 151, No. 4, 2022, pp. A118–A118. doi:10.1121/10.0010836.
- [37] Plotkin, K. J., Downing, M., and Page, J., “USAF Single Event Sonic Boom Prediction Model: PCBOOM,” *The Journal of the Acoustical Society of America*, Vol. 95, No. 5, 1994, pp. 2839–2839. doi:10.1121/1.409605.
- [38] Loubeau, A., and Coulouvrat, F., “Effects of Meteorological Variability on Sonic Boom Propagation from Hypersonic Aircraft,” *AIAA Journal*, Vol. 47, No. 11, 2009, pp. 2632–2641. doi:10.2514/1.41337.
- [39] Tannehill, J., Ievalts, J., and Lawrence, S., “An Upwind Parabolized Navier-Stokes Code for Real Gas Flows,” *26th Aerospace Sciences Meeting*, American Institute of Aeronautics and Astronautics, AIAA Paper 1988-713, 1988. doi:10.2514/6.1988-713.
- [40] Tannehill, J., Buelow, P., Ievalts, J., and Lawrence, S., “A Three-Dimensional Upwind Parabolized Navier-Stokes Code for Real Gas Flows,” *24th Thermophysics Conference*, American Institute of Aeronautics and Astronautics, AIAA Paper 1989-1651, 1989. doi:10.2514/6.1989-1651.
- [41] Tannehill, J., Buelow, P., Ievalts, J., and Lawrence, S., “A Three-Dimensional Upwind Parabolized Navier-Stokes Code for Real Gas Flows,” *24th Thermophysics Conference*, American Institute of Aeronautics and Astronautics, AIAA Paper 1989-1651, 1989. doi:10.2514/6.1989-1651.
- [42] Miller, J. H., Tannehill, J. C., and Lawrence, S. L., “Parabolized Navier-Stokes Algorithm for Solving Supersonic Flows with Upstream Influences,” *AIAA Journal*, Vol. 38, No. 10, 2000, pp. 1837–1845. doi:10.2514/2.865.
- [43] Vigneron, Y., Tannehill, J., and Rakich, J., “Calculation of Supersonic Viscous Flow over Delta Wings with Sharp Subsonic Leading Edges,” *11th Fluid and Plasma Dynamics Conference*, American Institute of Aeronautics and Astronautics, AIAA Paper 1978-1137, 1978. doi:10.2514/6.1978-1137.
- [44] Rubin, S. G., and Tannehill, J. C., “Parabolized/Reduced Navier-Stokes Computational Techniques,” *Annual Review of Fluid Mechanics*, Vol. 24, No. 1, 1992, pp. 117–144. doi:10.1146/annurev.fl.24.010192.001001.
- [45] Salvetti, A., and Seidman, H., “Noise and Sonic Boom Impact Technology. PCBOOM Computer Program for Sonic Boom Research. Vol. 2. Program Users/Computer Operations Manual.” *BBN LABS INC CANOGA PARK CA*, 1988.
- [46] Lonzaga, J. B., “Recent Enhancements to NASA’s PCBoom Sonic Boom Propagation Code,” *AIAA Aviation 2019 Forum*, American Institute of Aeronautics and Astronautics, AIAA Paper 2019-3386, 2019. doi:10.2514/6.2019-3386.
- [47] Page, J. A., Lonzaga, J. B., Shumway, M. J., Kaye, S. R., Downs, R. S., Loubeau, A., and Doebler, W. J., “PCBoom Version 7.1 User’s Guide,” *NASA Technical Reports Server*, 2020.
- [48] Cleveland, R. O., Chambers, J. P., Bass, H. E., Raspet, R., Blackstock, D. T., and Hamilton, M. F., “Comparison of Computer Codes for the Propagation of Sonic Boom Waveforms Through Isothermal Atmospheres,” *The Journal of the Acoustical Society of America*, Vol. 100, No. 5, 1996, pp. 3017–3027. doi:10.1121/1.417113.
- [49] Rallabhandi, S. K., and Loubeau, A., “Summary of Propagation Cases of the Second AIAA Sonic Boom Prediction Workshop,” *Journal of Aircraft*, Vol. 56, No. 3, 2019, pp. 876–895. doi:10.2514/1.c034805.
- [50] Rallabhandi, S. K., and Loubeau, A., “2nd Boom Prediction Workshop: Overview of Propagation Cases,” , 2017. URL https://1bpw-ftp.larc.nasa.gov/sbpw2/workshop/sbpw2-talks-propagation/01_Propagation_Workshop_Overview_Sriram.pdf, accessed 05/02/2023.

- [51] Bantle, J. W., "An Experimental and Analytical Study of the Aerodynamic Interference Effects Between Two Sears-Haack Bodies at Mach 2.7," *NASA-TM-85729*, 1985.
- [52] Juliano, T. J., Adamczak, D., and Kimmel, R. L., "HIFiRE-5 Flight Test Results," *Journal of Spacecraft and Rockets*, Vol. 52, No. 3, 2015, pp. 650–663. doi:10.2514/1.A33142.